Development, performance and energy trade-off analyses of wind turbine precipitation-reactive control at offshore and onshore sites in Western Europe

M. Sergio Campobasso[a,*], Matthew S. Rose[a], Sanshodhan Shende[b], Elisa Adirosi[c], Giandomenico Pace[d], Lorenzo De Silvestri[d], Krystallia Dimitriadou[e], Abhiram Vinod[e], Charlotte Bay Hassager[e], Fernando Sánchez[f], Alessio Castorrini[b,a]

[a]*School of Engineering, Lancaster University, Lancaster, LA1 4YW, United Kingdom.*
[b]*Department of Mechanical and Aerospace Engineering, Sapienza University of Rome, Rome, I00184, Italy.*
[c]*Institute of Atmospheric Sciences and Climate, National Research Council (CNR-ISAC), Rome, 00133, Italy.*
[d]*Laboratory Models and Measurements for Air Quality and Climate Observations, Italian National Agency for New Technologies, Energy and Sustainable Economic Development (ENEA), Rome, 00123, Italy.*
[e]*Department of Wind Energy, Technical University of Denmark, Roskilde, 4000, Denmark.*
[f]*Research Institute of Design, Innovation and Technology, University CEU Cardenal Herrera., CEU Universities, San Bartolome, 55, Alfara del Patriarca, 46115 Valencia, Spain.*

Abstract

Leading edge erosion of wind turbine blades increases Annual Energy Production (AEP) losses and maintenance. Precipitation-Reactive Control (PRC) curtails rotor speed during erosive precipitation events, alleviating erosion but incurring curtailment-induced AEP losses. Using novel methods combining accurate wind and rain measurements and computationally efficient algorithms to select optimal precipitation metrics to steer PRC, the trade-offs of AEP losses for curtailment and erosion at an onshore site in England (Lancaster-Hazelrigg), and a Mediterranean and North Sea offshore site are evaluated. All analyses use time-series of wind speed from cup, sonic or lidar anemometers, and droplet size distributions from laser beam disdrometers. Varying levels of AEP losses for erosion are considered. The assessment at the Mediterranean site, with low erosivity, shows that PRC enables 25+ years of erosion-free operation with a 0.07% curtailment-induced AEP loss, against a 1% loss for moderate erosion. At Lancaster-Hazelrigg, the three-year mean AEP loss of 1.3% considering curtailment and erosion losses is lower than with standard control. The doubled erosion-free life gives a net positive contribution to cost of energy reductions. At the North Sea site, the three-year mean total AEP loss with PRC is higher than without, indicating the need for long-term cost analyses to evaluate PRC viability.

Keywords: Precipitation-reactive control, Blade leading edge erosion, Energy yield losses for erosion and speed curtailment, Site-dependent trade-offs of energy yield losses, Optimization of rotor speed curtailment, Blade life extension for reduced cost of wind energy

*Corresponding author. e-mail: m.s.campobasso@lancaster.ac.uk

List of Abbreviations

AoA	Angle of Attack
AEP	Annual Energy Production
ALPS	AEP Loss Prediction System
DSD	Droplet Size Distribution
FDF	Frequency Distribution Function
GPM	Global Precipitation Measurement
IMERG	Integrated Multi-satellite Retrievals for GPM
LCOE	Levelized Cost of Energy
LE	Leading Edge
LEE	LE Erosion
LEP	LE Protection
LPM	Laser Precipitation Monitor
O&M	Operation and Maintenance
PDF	Probability Density Function
PRC	Precipitation-Reactive Control
SCADA	Supervisory Control And Data Acquisition
WARET	Whirling Arm Rain Erosion Test
WT	Wind Turbine

1. Introduction

Wind energy is playing a major role in decarbonizing electricity generation worldwide, and its role in this sector is rapidly gaining momentum. For example, China's government plans to more than double the country's current wind power capacity of 573 GW, 41 GW of which are contributed from offshore wind farms, to 1.3 TW by 2030. This foresees the installation of more than 120 GW of wind power per year, with at least 15 GW of this amount from offshore wind. An increasingly large deployment of offshore wind energy is being observed in several countries, due to a larger availability of the wind resource and its higher quality, *i.e.* lower turbulence intensity, offshore. In some countries, the growth of offshore wind parallels or exceeds that of onshore wind. For example, the UK aims to increase the current installed capacity of offshore wind of about 15 GW to 50 GW by 2030, and bring the present capacity of onshore wind of 15 GW to 30 GW by the same year. Achieving these goals requires optimizing all aspects of wind turbine (WT) maintenance and performance to reduce the Levelized Cost of Energy (LCOE). This requires reducing Operation and Maintenance (O&M) costs, which typically account for 25-30% of life-cycle LCOE [1], while maintaining or increasing wind farm Annual Energy Production (AEP).

This study focuses on the challenges posed by leading edge (LE) erosion of WT blades [2]. As explained below, LE erosion (LEE) reduces WT power and AEP, and increases maintenance interventions, with both occurrences hindering further reductions of wind LCOE. The presented research investigates the potential of an enhanced WT control strategy

to mitigate the detrimental impact of LEE on AEP losses and reduce blade maintenance frequency, along with the dependence of the benefit of this technology on the climatic conditions of the installation site.

LEE is caused by the repeated high-speed impact of rain droplets, hailstones or other airborne particles on the blade LE. The damage increases with particle mass and impact speed, and is thus highest in the outboard blade region, where the largest energy capture also occurs. Erosion yields LE geometry alterations that spoil the blade aerodynamic performance, *i.e.* reduce the lift force and increase the drag force acting on the blade, thus reducing rotor torque, power and AEP. From initial to intermediate stages, LEE reduces WT power due to premature laminar-to-turbulent transition of the blade boundary layer [3], and increased viscous and profile drag due to roughness [4]. At advanced stages, like that of the offshore WT depicted in Fig. 1, LEE reaches the composite substrate, jeopardizing the blade structural integrity. Furthermore, erosion depths become quite large, exceeding the height of the boundary layer height of the nominal blade airfoil. In this circumstance, small flow separations occur around the eroded area [5], which result in aerodynamic performance degradation and WT AEP losses often larger than those due to lower-amplitude and more distributed surface roughness [6]. Estimates based on Supervisory Control And Data Acquisition (SCADA) [7; 8] point to AEP losses of 2% or more onshore. Validated numerical analyses point to offshore losses of 2 to 2.5% [6; 4] for severe LEE. It is noted that even a small AEP loss yields significant revenue losses. For a wind farm of rated capacity of 1.2 GW and mean capacity factor of 45%, *e.g.* Hornsea 1 in the North Sea, a 0.5% AEP loss with LCOE of £50/MWh reduces revenues by about £1.2M per year.

Figure 1: Example of advanced LEE of offshore WT. Courtesy of iPS Powerful People.

LEE also increases wind farm O&M costs [9], which are notably higher offshore than onshore [10]. Blade erosion is the largest contributor to unplanned repairs, 12 times higher than structural failures [9]. The cost and health & safety challenges of WT condition monitoring and maintenance offshore may result in delaying maintenance until severe erosion compromises the blade structural integrity. Known major incidents due to LEE include the 2018 unplanned closure of the 630 MW London Array [11] and the 400 MW Anholt offshore wind farm [12].

The AEP losses before maintenance occurs, the cost of repairs and the associated turbine downtime, more significant offshore, pose a hard barrier to further LCOE reductions. LEE has become a major challenge in the wind energy sector, due to the unprecedented growth of offshore and onshore wind worldwide, including highly rainy regions in

East/Southeast Asia. Furthermore, rated blade tip-speeds are being increased to limit the growth of drivetrain loads and cost as rotor size grows [13], with the resulting higher tip speeds worsening LEE.

A significant effort has been recently made in developing erosion-resistant LE Protection (LEP) systems. These systems may belong to three main categories, namely liquid coatings, protective tape and erosion shields [2]. LEP systems improve LE durability, but do not entirely resolve the LEE challenge, particularly at installation sites characterized by frequent and intense precipitation.

A promising and complementary technology to mitigate LEE is the so-called "erosion safe WT operation" proposed in [14], called atmospheric Precipitation-Reactive Control (PRC) herein, in light of the emphasis of the presented research on the evaluation and optimization of the control steering variable. The key principle of PRC is to curtail the rotor angular speed when erosive precipitation events occur. This leads to a reduced impact speed of blade and hydrometeors, and, therefore, reduced LEE rate. Consequently, AEP losses due to reduced aerodynamic performance and maintenance downtime decrease; maintenance frequency and costs also decrease. Unavoidably, however, the speed curtailment yields reductions of the WT power during intense precipitation due to mechanical constraints on the maximum torque on the drivetrain, as explained in Section 2.1. One may expect that the economic viability of PRC increases as the frequency of intense precipitation events at high wind speed decreases [15]. Indeed, some studies indicate that PRC is an attractive option at sites where the LEE damage occurs over a small number of hours [16]. Investigating the general dependence of the PRC effectiveness in terms of LE life extension and AEP trade-offs is the key focus of this study. Previous key research in this sector includes the study of [17], who developed a deep reinforcement learning framework to optimize rotor speed considering rain-induced LEE. Using a surrogate model of the high-fidelity LEE analysis framework proposed in [18], the work of [17] determined the rotor speed for each wind speed and rainfall rate minimizing the AEP loss for speed curtailment and more than doubling the LE life of a 5 MW WT.

One of the challenges for the real-world deployment of PRC is the choice of the best suited steering parameters of this feed-forward control technology. The activation of PRC requires concurrent monitoring of the rotor angular speed and suitable precipitation parameters. In the case of rain-induced erosion, the droplet size is one of the key parameters affecting erosion rates [19]. However, the size of individual droplets cannot be used to steer PRC. One or more aggregated parameters of the precipitation, computed in real-time, are instead required. Assessing the site erosivity of the blade LE is required before evaluating the suitability of different aggregated precipitation metrics for steering PRC. In this regard, the study of [20], presented a multi-disciplinary multi-physics framework for blade LEE assessments that demonstrated the importance of using synchronous co-located time-series of measured wind speed and Droplet Size Distributions (DSDs) in LEE assessments. Measured DSD time-series are paramount to assessing site erosion potential [15], and analyzing AEP loss trade-offs in the PRC context. These data enable evaluating LEE progression rates with and without PRC, and determine the time-dependent LEE topographies [20] to estimate LEE-induced AEP losses [6]. When measured DSD time-series are not available, the empirical Best DSD [21] may be used. This model DSD depends only on the rainfall rate, and its validity is site-dependent, as shown below. This is because the measured DSD at two sites with a precipitation event featuring the same rainfall rate may differ.

The research presented herein addresses outstanding questions paramount to the real-world development of the PRC technology, including the dependence of its effectiveness on sites' climatic characteristics. More specifically, the main objectives of the study are to: a) accurately assess the blade erosivity of an existing onshore WT site, and prospective offshore wind farm sites in Western Europe making use of measured synchronous co-located wind speed and DSD time-series; b) apply prototype algorithms for evaluating performance and maximum theoretical efficiency of different precipitation metrics for PRC steering at the three sites; c) analyze the trade-off of AEP losses due to both rotor speed curtailment and LEE for given LE life extensions to quantify the potential of the PRC technology for reducing O&M, thus contributing to further LCOE reductions. To the best of the authors' knowledge, this is the first report investigating the choice of the best suited PRC steering parameter, performing parametric analyses of the technology's performance and efficiency using measured synchronous co-located wind speed and DSD time-series, and using such data for quantitative comparisons of the LE life extension and the AEP loss trade-offs at sites with significantly different climates.

All analyses refer to the case of LEE by rain, because this erosive agent is the most relevant to the considered sites, but can be generalized to the case of other erosive agents. The article is structured as follows. Section 2, Materials and methods, has three subsections: the definition of the multi-megawatt turbine used for all analyses is provided in Subsection 2.1, along with the alterations of the WT steady-state power curve and control trajectories for PRC; the erosion analysis method is summarized in Section 2.2, whereas the wind and rain data of the three selected sites are examined in Subsection 2.3, which also describes the instrumentation for the wind and rain measurements and defines the 1-year reference periods to which all analyses refer. Section 3, Results, consists of five parts: Subsection 3.1 quantifies the AEP losses of the considered WT due to moderate and severe erosion, whereas the blade erosivity of the three sites and the time to LEE onset are analyzed in Subsection 3.2. Here, droplet size Frequency Distribution Function (FDF) and map of fractional damage at the three sites are cross-compared to investigate the links between site climate and blade erosivity. The analyses are performed with both measured and Best DSDs to quantify the errors due to using an empirical DSD model when disdrometric data are not available. Subsection 3.3 analyzes the relative weight of droplet size and occurrence frequency on LEE damage and investigates the choice of the best suited rain parameter for PRC steering, whereas the optimal set-up of PRC, its site-dependent performance, and the AEP losses for rotor speed curtailment incurred to double the LE durability at the three sites are investigated in Subsection 3.4. The trade-offs of the AEP losses due to rotor speed curtailment and those due to LEE at the three sites are discussed in Subsection 3.5. Concluding remarks are provided in Section 4.

2. Methods and materials

2.1. Reference wind turbine and precipitation-reactive control

The analyses reported in this study use the IEA Wind 15 MW offshore reference WT [22]. The blades feature the FFA W3 airfoils. Hub height and rotor diameter are 150 m and 240 m, respectively. The blade geometry and the profile of the blade outermost airfoil, the FFA-W3-211 airfoil, are depicted in Fig. 2.

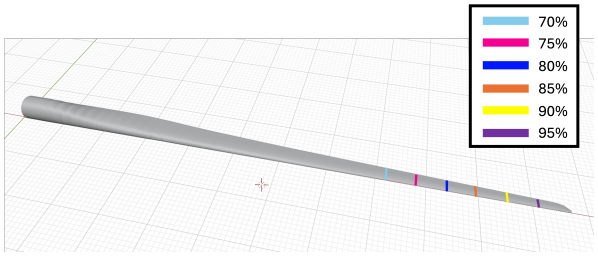

(a) Blade geometry with six radial positions at which LEE analysis is performed.

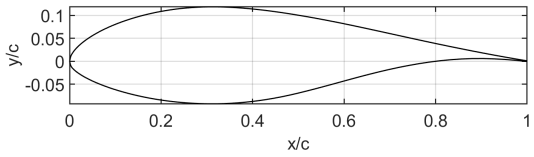

(b) FFA-W3-211 airfoil featured by outermost portion of IEA 15 MW WT blades.

Figure 2: Blade geometry of IEA 15 MW WT and FFA-W3-211 airfoil.

The cut-in, rated and cut-out wind speeds are, respectively, 3, 10.6 and 25 m/s, and the maximum tip speed is 95 m/s. The turbine is speed- and pitch-controlled; blade pitch control is collective and is active at start-up and above rated wind speed to maintain the power at its rated value; rotor speed control is instead used after start-up and until rated wind speed to maximize the WT power output. The IEA 15 MW WT has been modeled in OpenFAST [23] (version v3.5.3), an aero-servo-elastic framework for WT load and performance analyses. In this study, OpenFAST has been used to simulate the WT operation from cut-in to cut-out speeds without and with PRC. More specifically, it has been used to determine the curves of rotor speed N and blade pitch β versus wind speed V ($N-V$ and $\beta-V$ curve, respectively) without and with PRC, and also the curves of generator power P versus wind speed V in the two scenarios. The $N-V$ curves are needed to determine the relative impact speed of rain droplets and blade, which is one of the input variables needed for assessing the damage by rain erosion. The six radial positions at which the LEE analysis is performed are highlighted by the colored strips in Fig. 2a. Table 1 reports the numerical values of these positions as percentage values of the tip radius and in meters, along with the corresponding blade chords. In the OpenFAST analyses, wind

Table 1: Positions at which LEE analyses are performed and corresponding blade chords.

r [%]	70	75	80	85	90	95
r [m]	84.68	90.73	96.78	102.82	108.87	114.92
c [m]	3.22	3.00	2.77	2.52	2.26	1.99

turbulence has been neglected, and only wind shear, characterized by an exponent γ of 0.12 for the power law has been considered. Blade elasticity is resolved using the ElastoDyn library [24].

The steady-state curves of power P, aerodynamic torque Q and rotor thrust T without and with PRC determined with OpenFAST are reported in the top plot of Fig. 3, whereas those of rotor speed N and blade pitch β are depicted in the bottom plot of the same figure.

In both plots, dashed lines refer to standard operation, whereas solid lines refer to operation with rotor speed curtailment, *i.e.* with PRC. Rotor speed curtailment is activated at V=9 m/s, for reasons discussed in Section 3.2. The PRC operating conditions are determined by two constraints: one is that the reduced value of the maximum rotor speed should result in the maximum droplet/blade impact speed being at levels which reduce LEE; the other constraint is that

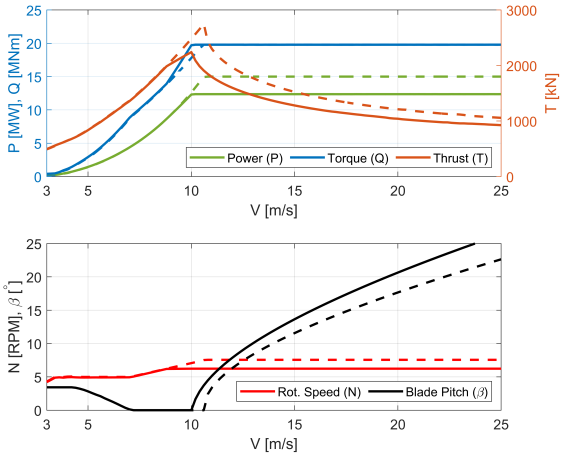

Figure 3: Steady-state power and load curves, and rotor control trajectories. Dashed lines refer to regular operation and solid lines refer to PRC operation. Top plot: generator power P, aerodynamic torque Q and rotor thrust T against wind speed V. Bottom plot: rotor speed N and blade pitch β against wind speed V.

the rotor torque should not exceed its rated value, *i.e.* the maximum value at which the WT operates with standard control. The fulfillment of these constraints is visible in Fig. 3. At V=9 m/s, the rotor speed N stops increasing, whereas the torque Q increases more rapidly than in standard operation mode, due to the Angle of Attack (AoA) increasing more rapidly. At $V \approx 10$ m/s, the rated torque is reached, and the pitch control starts pitching the blades to feather to keep the torque at its rated value by reducing the AoA as V increases. Blade pitching with PRC starts at lower wind speed V than in standard operation mode. It is noted that the use of rotor speed curtailment to reduce LEE may result in increased drivetrain fatigue, due to more frequent torque variations. The extent of this effect can be assessed with aeroservoelastic WT simulations which are part of the future extensions of the research presented herein.

To obtain the steady-state control trajectories with PRC for $V > 9$ m/s, OpenFAST has been wrapped by a MATLAB script that monitors the torque Q. As V increases above 9 m/s, the blade pitch is not changed until Q reaches its rated value. From the wind speed at which this happens, the script determines the value of the blade pitch angle β yielding the rated value of Q by means of a Newton-Raphson solution of the nonlinear problem.

The main operational parameters without and with PRC are reported in Tab. 2, in which V_r is the wind speed at which the maximum generator power P_{max} is achieved.

Table 2: WT operational parameters without and with PRC.

PRC	V_r [m/s]	N_{max} [RPM]	P_{max} [MW]	Q_{max} [MNm]	T_{max} [MN]
OFF	10.6	7.56	15.0	19.8	2.76
ON	10.0	6.23	12.4	19.8	2.24

2.2. Erosion analysis method

The model of the damage by rain droplet impact used to assess the erosion life of the LE coating is that proposed by [25]. The approach relies on the use of so-called $V_e - N_e$ curves of LEP systems measured in a Whirling Arm Rain Erosion Test (WARET) to improve the erosion life predictions of the empirical model due to Springer [26]. For each droplet impact speed V_e, which is the tangential velocity at a particular radial position of the three rotating arms bearing the LEP system in the WARET, N_e is the number of impacts per unit surface of droplets of given diameter leading to the end of the incubation period, *i.e.* the time at which erosion starts. The use of WARET data enables correcting key parameters of Springer's model [25; 20], resulting in enhanced reliability of its predictions.

In the LEE analyses herein, the non-normality of the droplet impact on the blade due to the airfoil curvature and velocity induction, which alters the relative air stream AoA and the trajectories of the impinging droplets, are not considered.

In the LEE model of this study, the impact area is assumed to be a small flat region of the LE, and variations of this area with the mean wind speed are neglected. The impact speed is taken to be the mean wind speed-dependent peripheral speed of the blade at the considered radial position along the blade, and the droplet impact is assumed normal to the LE. At each geographic site, the LEE analysis is performed over one year, using synchronous site-specific time-series of hub-height wind speed and DSD. Both wind speed and DSD time-series use a time-step of 10 min. The blade peripheral speed $v_s(t)$, taken to be constant over each 10-min interval, is calculated for each mean wind speed V by using the steady-state $N-V$ curve computed before the erosion analysis. The number of droplets n'_s of diameter D per m^2 impacting the LE in each 10-min interval is:

$$n'_s(D, v_s(t)) = 600\, v_s(t) n'_v(D,t) \tag{1}$$

where $n'_v(D,t)$ denotes the number of droplets of diameter D per m^3 in the precipitation in the considered 10-min interval. To determine the damage $D'_s(D, v_s(t))$ in the considered interval, the number of impacts per unit surface $N_s(D, v_s(t))$ that would lead to the end of the incubation period with all impacts characterized by droplets of diameter D hitting the LE at speed $v_s(t)$ is also needed. This parameter is determined using the approach of [25]. The overall damage $D_{s,T}$ over the reference period of 1 year is then obtained by accumulation using the Miner-Palmgren rule, that is:

$$D_{s,T} = \sum_{i=1}^{M_I} \sum_{j=1}^{N_D} D'_{s,ij} = \sum_{i=1}^{M_I} \sum_{j=1}^{N_D} \frac{n'_{s,ij}}{N_{s,ij}} \tag{2}$$

where subscript i and j are the indices of the 10-min interval and droplet bin, respectively. Symbols M_I and N_D denote the total number of 10-minute intervals with rain and the number of D bins, respectively. The coating durability in years is $L_c = 1/D_{s,T}$. The calculation of $D_{s,T}$ requires the time-series of V and DSD, since the value of $n'_s(D, v_s(t))$ in each 10-min interval depends on the measured value of V, due to the dependence of $v_s(t)$ on V, and the measured value of $n'_v(D)$.

The LEP selected for the analyses of this study is a 3M liquid coating made up of polyurethane. The material properties of this LEP system, based on WARET data, are provided in Appendix A, and their derivation is presented in [27].

It is noted that higher-fidelity LEE analysis methods could be adopted, such as that of [18], using Smooth Particle Hydrodynamics and finite element analysis to determine the coating stress due to water droplet impacts, and also adopting alternative fatigue analysis approaches. This is part of future extensions of the present work.

2.3. Selected onshore and offshore sites

Three sites are considered in the LEE and PRC analyses herein. The first site, onshore, is the Hazelrigg site in Northwest England on Lancaster University premises. A 2.3 MW WT and a UK Met Office weather station are operational at the site, a view of which is reported in Fig. 4a. The second site is in the Southern Mediterranean. It is the offshore site where the ENEA Station for Climate Observation on the island of Lampedusa is located [1]. Lampedusa is a small island with area of about 20 km^2, located about 130 and 215 km from Tunisia and Sicily, respectively. The prevailing wind direction is from the northwest, and the island has a fairly flat terrain. The prevailing wind direction is from the northwest and the weather station is on the northeastern coast of the island. The ENEA station hosts also a weather station, which includes a 10-meter mast, and a disdrometer. A view of the met mast and the surrounding area, where the disdrometer is also located, is reported in Fig. 4b. The third site, also offshore, is in the North Sea (NS) off the western coast of Germany. A view of the buoy hosting a wind LiDAR and a weather station at the site is reported in Fig. 4c.

The geographical location of the three sites is indicated in the map of Fig. 5, whereas their latitude and longitude are provided in Tab. 3. The LEE and PRC analyses of this study consider a period of one year (reference period) for all three sites. The start and end dates of the reference periods are also reported in Tab. 3.

Table 3: Reference periods for LEE and PRC analyses at selected sites.

Site	Latitude	Longitude	Start date	End date
Lancaster	54.0138° N	2.7749° W	October 2018	September 2019
Lampedusa	35.518° N	12.630° E	January 2024	December 2024
NS site	54.4029° N	5.5211° E	March 2022	February 2023

For all three sites, one-year wind speed time-series with time-step of 10 min at the hub height of 150 m are used. At Lancaster, the wind speed time-series at 150 m height has been obtained from that recorded by the cup anemometer of the 2.3 MW WT at the site over the reference period. The output frequency of the measurements is 10 min. Since the nacelle is at 64 m height, the wind speed at 150 m has been obtained by extrapolations based on the power law of the vertical wind profile,namely $V = V_{ref}\left(z/z_{ref}\right)^{\gamma}$. To improve accuracy, the exponent γ has been calculated for each set of six consecutive 10-min intervals using the values computed from the hourly wind speeds at 10 and 100 m provided by the ERA5 repository of global climate reanalysis [28].

At Lampedusa, the wind speed time-series at 150 m height over the reference period has been obtained from that recorded by the Vaisala WINDCAP Ultrasonic WMT700 sonic anemometer - part of a Vaisala Milos 500 weather

[1] https://www.lampedusa.enea.it.

(a) Hazelrigg weather station and campus WT.

(b) Lampedusa met mast.

(c) Buoy-fitted wind LiDAR used at North Sea site. Courtesy of ZX Lidars.

Figure 4: Images of instrumentation at three selected sites.

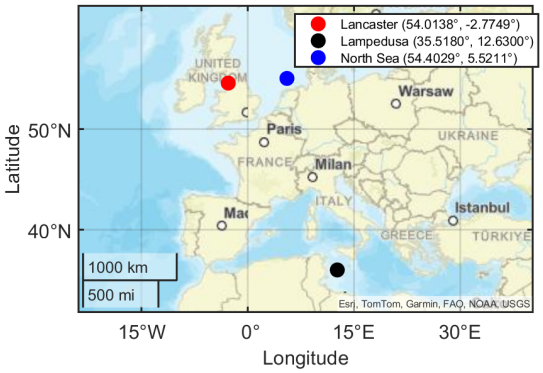

Figure 5: Geographic location of three selected sites.

station - on the 10-m met mast. Since the output frequency of the measurements is 1 min and the time-series for the LEE and PRC analyses is 10 min, the required time-series have been obtained by data aggregation, that is taking the mean wind speed of each set of 10 consecutive 1-min measurements. The exponent γ needed to extrapolate the measured wind speed at 150 m has been calculated using ERA5 data, as for the Lancaster site.

At the NS site, the wind speed time-series at 150 m height over the reference period has been obtained from that recorded by a buoy-fitted offshore LiDAR anemometer (model ZX300M) over the same period [29]. The output frequency of the wind measurements is 10 min. Measured wind speeds are available at 140 and 200 m. Thus, the wind speed at 150 m has been obtained by power law interpolations, and the exponent γ has been calculated for each 10-min interval using the measured wind speeds at 140 and 200 m.

The scale factor c and the shape factor k of the Weibull Probability Density Function (PDF) at the three sites, along with the mean annual wind speed, are reported in Tab. 4. An ERA5-based verification of the wind measurements used for the LEE and PRC of this study is provided in Appendix B.

Table 4: Weibull PDF scale factor c and shape factor k, mean annual wind speed V_{mean} and annual rainfall T_A at selected sites. PDFs based on 10-min wind data bins at 150 m. Lancaster and Lampedusa annual rainfall T_A based on disdrometric readings and North Sea T_A based on IMERG data.

Site	c [m/s]	k [-]	V_{mean} [m/s]	T_A [mm]
Lancaster	8.02	1.89	7.1	1193
Lampedusa	9.00	1.74	8.0	190
NS site	11.27	2.17	9.9	1260

For all three sites, measured time-series of the rainfall rate R over the reference periods are available, and also measured DSD time-series are available for the Lancaster and Lampedusa sites. Since disdrometric data are not available at the NS site, the DSD time-series at this site are computed using the empirical Best DSD [21], which depends on the rainfall rate R. The required R time-series is obtained from NASA's Integrated Multi-satellite Retrievals for GPM (IMERG) [30] database. The T_A value for the NS site in Tab. 4 is also calculated with the IMERG data.

All LEE and PRC analyses in this study use DSDs measured or computed every 10 min. At the Lancaster Hazelrigg and Lampedusa sites, a Thies Clima^{TM} Laser Precipitation Monitor (LPM) [31] has been used to measure the DSD time-series over the reference period. Since the LPM has data output frequency of 1 min and the time-series for the LEE and PRC analyses use a time-step of 10 min, these latter have been obtained by aggregating the data of sets of ten consecutive 1-min LPM readings.

At Lancaster and Lampedusa, the R time-series, needed for LEE and PRC analyses using the Best DSD, have been computed using the disdrometric data, as explained in Appendix B. These time-series are also used to determine the annual rainfall T_A reported in Tab. 4. At the NS site, the 10-min R time-series for the reference period is obtained from IMERG, by assuming R to be constant over three consecutive 10-min intervals, as the time-step of the original IMERG time-series is 30 min. For cross-validation purposes, the R frequency occurrence of the three sites using all available data sources, *i.e.* ground- and satellite-based measurements, are compared in Appendix B.

An important parameter used to both qualitatively characterize the site precipitation regime and, potentially, also to steer WT PRC, is the mass-weighted mean diameter D_M, whose definition is:

$$D_M = \frac{\int_{D_{min}}^{D_{max}} N_x(D) D^4 dD}{\int_{D_{min}}^{D_{max}} N_x(D) D^3 dD} \tag{3}$$

Here, D is the droplet diameter, N denotes DSD, and subscript 'x' is 'M' for measured and 'B' for Best DSDs. The curves of D_M against R over the considered reference periods at Lancaster and Lampedusa are reported in Fig. 6. The two symbol clouds provide the values of D_M calculated for each 1-min observation for the measured R, and the figure also reports a power law fitting of the measurements at the two sites. The D_M curve based on the Best DSD is also reported for reference. One notes that at Lampedusa the Best DSD fits fairly well the mean characteristics of the observed precipitation for $R > 1$ mm/hr. At lower R levels, the agreement worsens, indicating possible larger discrepancies between the model DSD and the DSD associated with the actual precipitation. At the Lancaster site, conversely, the Best curve overpredicts D_M over the entire R range considered. These trends indicate that the Best DSD is biased towards larger droplets for all R values at Lancaster, whereas it better matches the relative amounts of droplets

of different size at Lampedusa. These differences, examined in greater detail in Appendix B, are key to LEE and PRC analyses, as the droplet size is one of the key parameters affecting erosion rate and, in turn, AEP losses due to LEE and PRC-linked rotor speed curtailment.

The trends above point to the fact that at sites with a predominantly convective rain regime, like Lampedusa, LEE analyses may be performed measuring only R and, potentially, PRC may also be implemented by measuring only R. Conversely, at sites like Lancaster, the use of disdrometric data may be essential to avoid errors in estimating AEP losses due to LEE and rotor speed curtailment in PRC assessments. These aspects are discussed in greater detail in Sections 3.2 and 3.4.

The discrepancies between Best and measured DSDs at some wind farm sites have been observed in other studies. For example, notable differences between the two DSDs have been found at an offshore site in the NS close to the northeastern coast of England [32]. The large scatter in the measured data of Fig. 6 is a consequence of the temporal anisotropy of rain precipitation. Both the temporal and spatial anisotropy of rain precipitation may be accounted for in LEE assessments by using stochastic models like that demonstrated in [33].

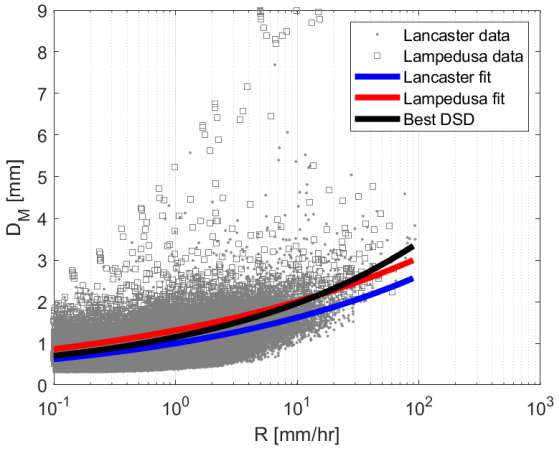

Figure 6: Measured and Best DSD-based mass-weighted mean diameter D_M versus rainfall rate R.

3. Results

In this section, the analyses of the AEP losses due to LEE and those incurred for rotor speed curtailment when using PRC are performed for the three sites under investigation. The selected turbine is the IEA 15 MW WT in all cases.

3.1. AEP losses due to LEE

To produce quantitative terms of reference for the AEP losses due to rotor speed curtailment with PRC, the AEP losses due to LEE incurred with standard operation mode are determined in this section. The AEP Loss Prediction System (ALPS) [6] has been used to determine the LEE-induced AEP losses caused by one moderate and one severe LEE state. The ALPS calculation of the AEP loss requires estimating the aerodynamic performance of both the

nominal blade and the two eroded blade variants. Since the rotor performance is determined with the implementation of the blade element momentum theory embedded in OpenFAST, the AEP loss assessment requires the curves of lift coefficient c_l and drag coefficient c_d against the AoA for the nominal and eroded blade airfoils [6].

Both moderate and severe erosion are assumed to cover the outermost part of the blade, from the tip to 70% rotor radius. Although the IEA 15 MW WT uses the FFA-W3-211 airfoil from the blade tip to 76% rotor radius, the ALPS analyses below assume that this airfoil is used until 70.4% for simplicity, as this enables analyzing a single airfoil for each of the three blade variants. It has been verified that this approximation introduces negligibly small variations of the clean turbine AEP with respect to when the actual blade geometry of the IEA 15 MW WT is used.

The moderate erosion state features distributed LE roughness with equivalent sand grain roughness k_s [34] of $k_s = 200$ μm, referred to a 1-meter chord, extending from the LE to 13% chord on the lower side and from the LE to 3% chord on the upper side. The considered level of moderate erosion depth corresponds to damage of the LE coating, insufficiently deep to affect the composite substrate of the LE. The severe LEE damage is based on a constant-depth chordwise groove affecting both the upper and the lower areas of the LE, a model also used for uncertainty analysis of the LEE topography in [5]. The groove starts at 13% chord from the LE on the lower side and ends at 5% chord from the LE on the upper side, and has depth of 1.5 mm referred to a 1-meter chord. Additionally, distributed roughness of 200 μm is applied to the groove to account for the additional detrimental impact of the rough surface of the partially eroded composite substrate on aerodynamic performance.

Computational Fluid Dynamics (CFD) is used to determine the c_l and c_d curves of the clean and eroded FFA-W3-211 airfoils for a reference chord- and relative speed-based Reynolds number of 10M. This value is that indicated for this airfoil in the definition of the IEA 15 MW [22]. For given rotor speed, the Reynolds number varies by less than 20% between 55 and 95% blade tip radius. The value of 10M corresponds to the Reynolds number level in this blade region at $V \approx 8$ m/s. Since the AoA values of the outboard blade portion, which harnesses the majority of the wind power, is well below stall in the operating range with constant tip-speed-ratio, the value of 10M turns out to be an adequate choice for assessing the performance of the outboard blade over the entire wind speed range. ANSYS Fluent [35] version 2024 R2 is used for the simulations. All CFD analyses are incompressible and two-dimensional, and solve the Reynolds-averaged Navier-Stokes coupled to the Shear Stress Transport $k-\omega$ turbulence model [36]. The simulations of the clean airfoil use a grid with 370880 cells, and integrate the transport equations of the turbulence model down to the wall. The clean airfoil analysis of the FFA-W3-211 airfoil is performed using a free transition model of surface boundary layers [37], whose set-up is described in [3]. It has been verified the maximum value of the minimum nondimensionalized wall distance y^+ is below 0.5 at all AoA values considered.

The simulations of the airfoil with moderate erosion use the same airfoil geometry and grid of the clean airfoil case. Furthermore, a distributed roughness model [3; 4], based on the equivalent sand grain roughness [34], is used to account for the effects of LEE in aerodynamic performance. The CFD simulations of the airfoil with severe LEE assume fully turbulent boundary layers, since the geometrically resolved forward facing steps of the LE groove [5] trip the boundary layers at the LE [4]. It has been verified that the grids used for the simulations of all three airfoil variants produce grid-independent results.

The force coefficients of the clean FFA-W3-211 airfoil and its two eroded variants are compared in Fig. 7. Figure 7a reports the curves of c_l against the AoA α, whereas the drag polars are compared in Fig. 7b. As expected, the aerodynamic performance impairment increases significantly with LEE severity. The AoA at the outboard part of the blades of the IEA 15 MW WT for wind speed V between 6 and 10 m/s varies between about 7.2° and 7.5°. Comparing the aerodynamic performance at $\alpha = 8^{\circ}$, a representative value accounting also for AoA increases in the presence of LEE, one sees that the c_l value of the clean airfoil of 1.21 decreases to 1.15 with moderate LEE and down to 1.09 in the case of severe LEE. The increase of the drag force is also significant: the nominal c_d value of 0.010 increases to about 0.015 with moderate LEE and up to 0.021 with severe LEE.

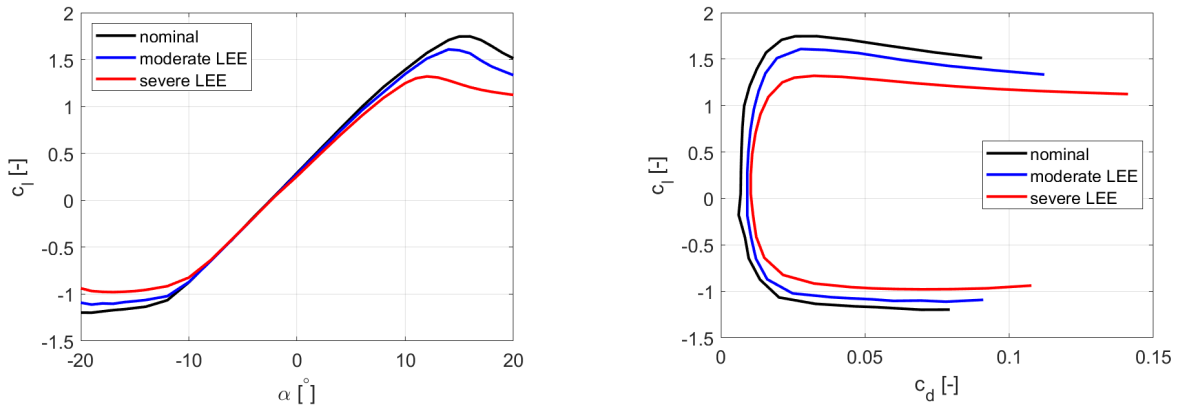

(a) Lift coefficient c_l versus AoA α.

(b) Lift coefficient c_l versus drag coefficient c_d.

Figure 7: Force coefficients of nominal FFA-W3-211 airfoil and two variants with moderate and severe LEE.

The reduction of aerodynamic performance highlighted above results in reductions of WT power and AEP. The power curve of the nominal and eroded WTs are determined with OpenFAST, using the analysis set-up with standard control summarized in Section 2.1. These assessments do not consider atmospheric turbulence for consistency with the analyses of the AEP losses for rotor speed curtailment of Section 3.4, which also neglect this feature. The adopted c_l and c_d curves of the nominal and eroded FFA-W3-211 airfoils used in the outboard part of the blades are those discussed above, and the force coefficients of all other airfoils are those reported in [22]. The wind data used to determine all AEP values at the three sites are those presented in Section 2.3. The AEP values of the nominal IEA 15 MW WT with standard control at the three sites are reported in Tab. 5.

Table 5: AEP at three selected sites for ideal case, *i.e.* standard operation (no PRC) and blades unaffected by LEE.

Location	Lancaster	Lampedusa	North Sea site
AEP (MWh)	49561	56433	77923

The AEP losses associated with the moderate and severe LEE states at the three sites are provided in Tab. 6. These data indicate that, for given LEE state, the AEP loss is largest at Lancaster and smallest at the NS site. This is because the mean annual wind speed at the former site is lower than at the latter. In general, the blade pitch control, whose main

Table 6: AEP losses due to moderate and severe LEE at three considered sites.

		Lancaster	Lampedusa	North Sea
$(\text{AEP loss})_{\text{LEE}}$ [%]	Moderate LEE	1.37	1.00	0.77
	Severe LEE	2.74	1.98	1.56

task is maintaining the output power constant and equal to the rated value above rated wind speed, compensates for the c_l reduction and c_d increase due to LEE by pitching the blades of a WT hit by LEE less than those of the corresponding WT with clean blades [4]. This occurrence makes the power curve insensitive to LEE once the rated power is achieved. Since the damaged WT at the NS site spends more time above rated wind speed than the same WT at Lancaster, the percentage AEP loss at the former site is smaller than that at the latter site. It is also noted that LEE slightly increases the wind speed at which the eroded WT achieves rated power. This increase, however, is notably smaller than the mean annual wind speed increase of nearly 3 m/s at the NS site, as reported in Tab. 4, making the latter feature the leading effect in the variation of the percentage AEP loss. Finally, one notes that, for given site, the AEP loss increases with the LE damage severity, as expected.

3.2. Analysis of site erosivity of the blade LE

The analyses of site erosivity of the blade LE herein aim at estimating the time taken for LEE to appear, *i.e.* the time from which the AEP losses determined in the previous section are incurred. The LEE assessment of the 15 MW WT uses the method defined in Section 2.2. The adopted time-series of wind speed and DSDs are those described in Section 2.3.

In order to more easily compare the characteristics of the synchronous wind speed and DSD data of the three sites, the left plots of Fig. 8 present the sites' joint FDFs of the droplet size relative frequency. The independent variables are wind speed V and droplet diameter D. These FDFs have been generated by using 10-min time-series of wind speeds and DSDs over the reference period of each site. The relative frequency $n_v/n_{v,T}$ is the ratio of the total number of droplets per m^3 n_v of a particular $V-D$ bin in the reference period and the total number of droplets per m^3 $N_{v,T}$ in the same period. The first droplet class ($0.125 < D < 0.250$ mm) has not been considered in the generation of the three maps, due to uncertainty affecting disdrometric readings of very small and very large droplets [38; 39; 40].

The droplet size FDF at Lancaster (Fig. 8a) indicates that the largest amount of droplets is in the region with $D < 1$ mm and $V < 15$ m/s. The corresponding FDF at Lampedusa (Fig. 8c) is qualitatively similar to that at Lancaster, but it indicates larger proportions of droplets with $1 < D < 3$ mm. This difference is consistent with the analysis of Appendix B. Furthermore, the Lampedusa site has rain at low wind speed with respect to Lancaster. The droplet size FDF of the NS site (Fig. 8e), using measured wind but IMERG R data and the Best DSD, is remarkably different from the other two maps, as it indicates large amounts of rain at wind speeds well above 20 m/s.

The results of the erosion analyses at the three sites based on the wind and rain time-series are reported in Tab. 7. For Lancaster and Lampedusa, Tab. 7 also reports the coating lives obtained by adopting Best DSD time-series generated

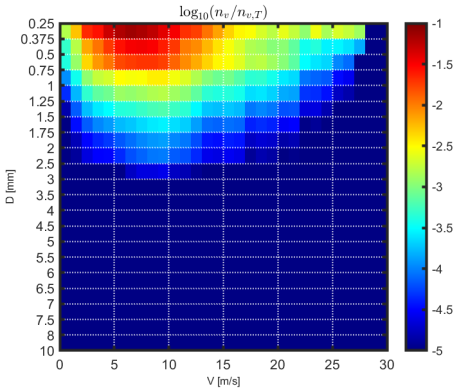

(a) Lancaster: droplet FDF based on measured wind and measured DSD time-series.

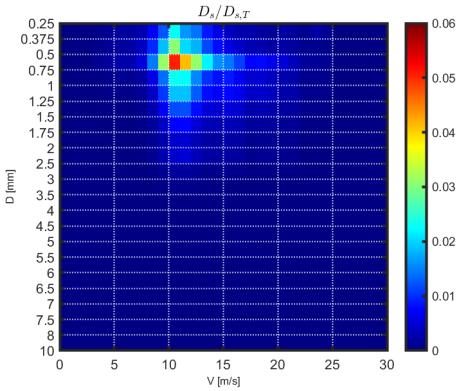

(b) Lancaster: fractional damage FDF based on measured wind and measured DSD time-series.

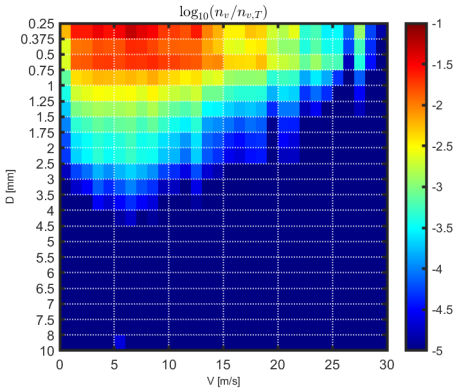

(c) Lampedusa: droplet FDF based on measured wind and measured DSD time-series.

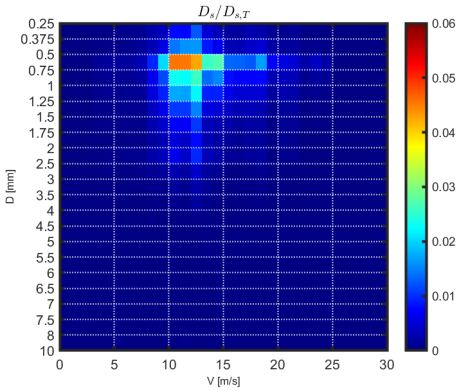

(d) Lampedusa: fractional damage FDF based on measured wind and measured DSD time-series.

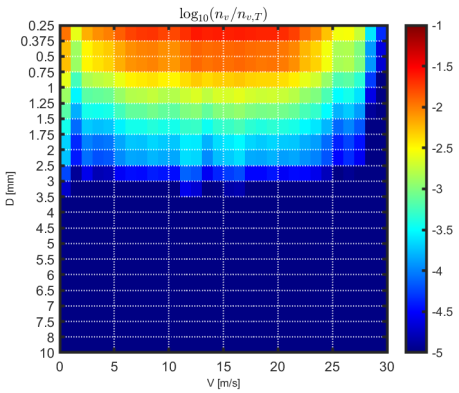

(e) North Sea site: droplet FDF based on measured wind and Best DSD using IMERG *R* time-series.

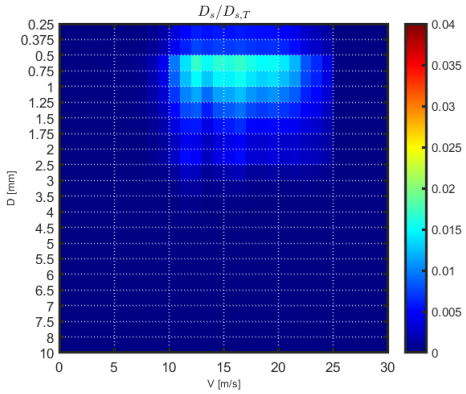

(f) North Sea site: fractional damage FDF based on measured wind and Best DSD using IMERG *R* time-series.

Figure 8: Normalized joint FDFs of droplet count (left), and corresponding joint FDF of LE fractional damage at 95% rotor tip (right) at three sites.

Table 7: LE coating lifetime prediction at six blade positions of Tab. 1 at three selected sites.

r [%]	70	75	80	85	90	95
Life [yr] - Lancs./Meas.	13.0	7.3	4.2	2.5	1.6	1.0
Life [yr] - Lancs./Best	16.6	9.3	5.4	3.3	2.0	1.3
$\Delta\text{Life}_{M/B}$ [%]	-22.8	-22.8	-22.8	-22.8	-22.8	-22.8
Life [yr] - Lamp./Meas.	180.4	101.0	58.7	35.3	21.8	13.8
Life [yr] - Lamp./Best	167.3	93.7	54.4	32.7	20.2	12.8
$\Delta\text{Life}_{M/B}$ [%]	+7.8	+7.8	+7.8	+7.8	+7.8	+7.8
Life [yr] - NS/Best	9.9	5.5	3.2	1.9	1.2	0.75

with the measured R of each 10-min interval, and also the percentage difference between the lives evaluated using measured and Best DSD time-series. For each site and DSD type, the table reports the incubation times at the six blade positions in Tab. 1. The shortest coating life is always that at 95% tip radius, characterized by the largest blade/droplet relative impact speeds. Based on measured DSDs, LE erosivity at Lancaster is substantially higher than at Lampedusa, as the coating life at 95% tip radius is 1 year at the former site and 13.8 years at the latter one. This is for two reasons: one is that the annual rainfall at Lancaster in the reference period is six times larger than at Lampedusa, and the other is that at Lampedusa a significant amount of the annual precipitation occurs at low wind speed with respect to Lancaster (rain at low wind speed is less erosive due to lower rotor speed). The NS site is even more erosive than Lancaster, as the coating life at 95% tip radius is only 0.75 years. The coating life at the NS site is the lowest of the three sites because it experiences the largest annual rainfall and the largest proportion of intense precipitation at high wind speed.

The use of the Best DSD at Lancaster leads to an overestimation of about 23% of coating lives, whereas at Lampedusa the use of the empirical DSD model underestimates by about 8% coating lives. The fact that the magnitude of this difference is smaller at Lampedusa is due to the fact that at this site the measured and Best DSDs are closer than at Lancaster, as observed in Appendix B. The more optimistic estimate of the Best DSD-based LEE analysis at Lancaster is due to the fact that the Best model underestimates the amount of small droplets and, consequently, their contribution to LEE. The overestimation of the medium-sized droplets and their contribution to LEE does not outweigh the impact of the small droplets. At Lampedusa, conversely, Best underprediction of the small droplets is notably smaller than at Lancaster. The effect of the overestimation of the medium-sized particles on LEE prevails over the underestimation of small droplets, and the predicted coating life is thus sightly shorter than that based on the measured DSDs.

The analyses above highlight both the large differences in LEP system durability arising from different wind and rain climates, and the site-dependent agreement of measured and model DSDs. The latter point is particularly relevant to the development of the WT PRC technology and the minimization of AEP losses due to rotor speed curtailment, as discussed in Section 3.4.

The right plots of Fig. 8 report the joint FDFs of the fractional erosion damage $D_s/D_{s,T}$ at 95% tip radius corresponding to the droplet size FDFs of the three sites in the left plots. These damage maps have been generated using the output of the LEE analyses making use of the 10-min time-series of wind speeds and DSDs over the reference period.

The fractional damage is the ratio of the damage D_s caused in the reference period by all the droplets in a particular $V-D$ bin and the overall damage $D_{s,T}$ in the same period. The damage D_s in the reference period is computed by accumulating the damage D'_s occurring in each 10-min interval of the time-series in the considered $V-D$ bin. The definition of D'_s is provided by Eq. (2).

The fractional damage map of Fig. 8b shows that at Lancaster significant damage starts at a wind speed V of 9 m/s, with the peak damage occurring for $10 < V < 11$ m/s (around rated wind speed) and $0.5 < D < 0.75$ mm, a relatively small droplet size. The fractional damage for $V > 15$ m/s is very small. At Lampedusa (Fig. 8d), trends are similar. Also in this case the peak damage occurs around the WT rated wind speed and for small droplet sizes. The most notable differences are a higher damage produced by small droplets ($0.25 < D < 0.5$ mm) at Lancaster and a higher damage produced by larger droplets ($0.5 < D < 1.25$ mm) at Lampedusa. Both findings are in line with the D_M analysis of Fig. 6 and the rain data analyses of Appendix B. The fractional damage map of the NS site is remarkably different from that of the other two sites, as significant erosion damage is observed all the way up to $V \approx 22$ m/s. This is because the amount of rain at high wind speed is larger than at the two other sites.

3.3. PRC steering parameters and activation thresholds

This section discusses the choice of a suitable precipitation-related metric to steer PRC. The individual droplet diameters cannot be used for steering PRC, as a wide range of droplet sizes exists in each rain event. Conversely, PRC steering requires using an integral or mean parameter featuring a good correlation with the erosion damage determined with measured DSD time-series. For each candidate parameter, a method to determine its threshold value for activating PRC is also required, an issue also addressed in this section. The problems of selecting suitable PRC steering parameters and determining their threshold values are addressed by considering the Lancaster site.

The relationship between different measured rain parameters and erosion damage at the Lancaster site is analyzed in Fig. 9. Figure 9a reports the joint FDF of the normalized droplet count, whereas Fig. 9b provides the corresponding FDF of the fractional damage (these two figures are the same maps of Figures 8a and 8b). It is noted that the fractional damage of Fig. 9b accounts for both the erosivity of each droplet of diameter D at wind speed V, and the number of impacts of this type. To examine separately these two effects, one can also determine a joint FDF of erosivity or specific fractional damage by dividing the value of each bin of the map of Fig. 9b by the number of impacts with the V and D values of that bin, *i.e.* by the corresponding value of the map of Fig. 9a. In the region with precipitation, the resulting map (not reported for brevity) shows that, for given V, erosivity increases monotonically with the droplet size D, in line with the WARET observations [14]. Hence, the occurrence of the peak fractional damage at $10 < V < 11$ m/s and $0.5 < D < 0.75$ in Fig. 9b does not mean that this droplet class is the most erosive one, but merely that the erosivity of these droplets combined with their high occurrence frequency yields the largest fractional damage of the reference period.

The mass-weighted mean diameter D_M is one of the possible parameters usable to steer PRC. The map of Fig. 9c presents the relative frequency of occurrence of D_M over the reference period, with symbols n_{DM} and M_I denoting, respectively, the number of 10-min intervals of each $V-D_M$ bin, and the overall number of 10-min intervals with rain detected. For each 10-min interval, D_M is computed with Eq. (3). The fractional damage map of Fig 9d differs

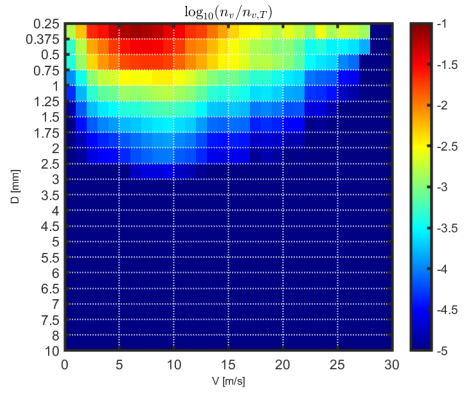

(a) Normalized FDF of droplet count.

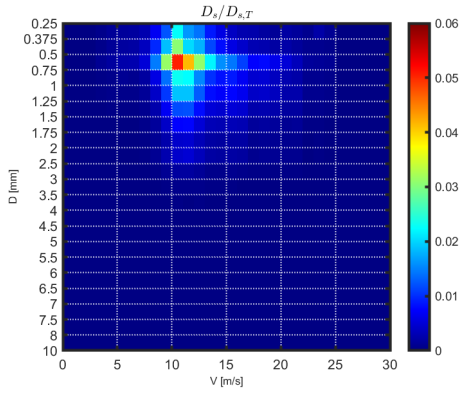

(b) Fractional damage FDF based on V and D.

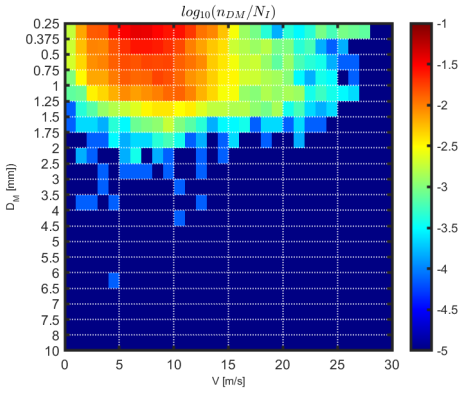

(c) Normalized FDF of measured DSD-based D_M count.

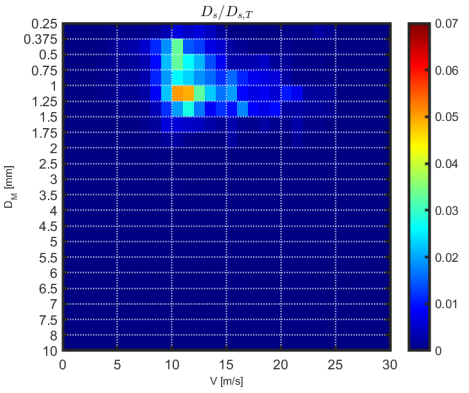

(d) Fractional damage FDF based on V and D_M.

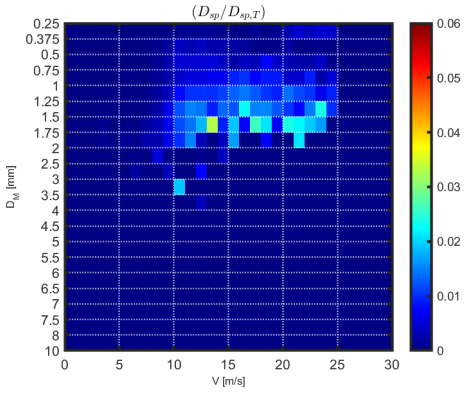

(e) Specific fractional damage FDF based on V and D_M.

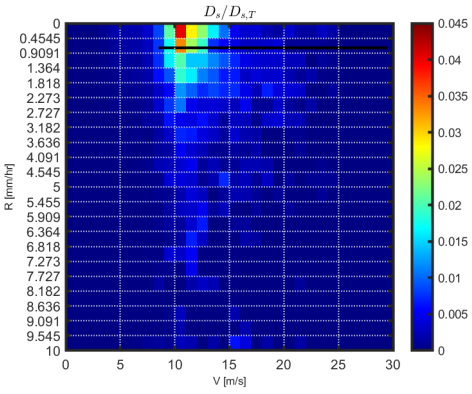

(f) Fractional damage FDF based on V and R.

Figure 9: Joint FDFs of droplet count and corresponding mass-weighted mean diameter count, and fractional damage and specific fractional damage based on D, DSD-based D_M and R at Lancaster. All maps based on measured wind and measured DSD time-series.

from that of Fig. 9b in that the former uses D_M as rain parameter, whereas the latter uses the droplet diameter D. The fractional damage map of Fig. 9d shows that the peak fractional damage $D_s/D_{s,T}$ occurs at $1.0 < D_M < 1.25$ mm and $10 < V < 15$ m/s.

The fractional damage map of Fig. 9d considers both the erosivity of a 10-min rain event at given D_M and v, and the occurrence frequency of that event. Also when using D_M as integral rain parameter, one can obtain a specific damage joint FDF. This is accomplished by by dividing each bin of the damage map of Fig. 9d by the corresponding bin of the map of Fig. 9c. The operation yields the normalized specific damage joint FDF of Fig. 9e. More specifically, this map is obtained by dividing the map of non-normalized damage D_s by that of D_M occurrence, which yields a map of specific damage D_{sp}. This latter is then normalized by the total specific damage $D_{sp,T}$, yielding the FDF of Fig. 9e. It is noted that, for given V, the specific damage does not increase significantly with D_M, as expected. Moreover, for $1.25 < D_M < 1.75$ mm, multiple gaps are encountered as the wind speed increases from 11 to 20 m/s. This is also unexpected, since the rotor speed in this V range is constant and rainfall occurs over the whole V range, as visible in Fig. 9c. Both phenomena are linked to the wide scatter of the measured DSD-based D_M data visible in Fig. 6. As discussed in greater detail below, this scatter results in the number of larger and more erosive droplets not always increasing with the value of D_M of the 10-min precipitation. On the other hand, if the specific damage map is plotted by using values of D_M computed with the (analytical) Best DSD, but still using the measured DSDs for the LEE analysis, the specific damage map shows that, for given V range, the specific damage increases monotonically with D_M. These observations are important for the discussion of the PRC analyses of Section 3.4.

Another possible PRC steering parameter is the measured rainfall rate R. An advantage of using this variable over the D_M parameter computed in real-time with measured-DSD time-series is the avoidance of disdrometric measurements. The joint FDF of the fractional damage as function of V and R is shown in Fig. 9f. Also in this case, the erosion analyses are performed using the measured DSDs. The largest fractional damages are observed at the lowest R levels. This is because the reported damage considers both the erosivity of the rain events (with each event defined by a bin's R and V values), and their occurrence frequency. The high damage at low rainfall rate R is due to the high occurrence of moderately erosive rainfall.

Since LEE damage becomes significant at $V = 9$ m/s at all three considered sites, all PRC analyses reported herein apply rotor speed curtailment from this wind speed. The second condition for activating PRC is determined by the value of a precipitation-related parameter. An algorithm based on the Secant method (Algorithm A in Appendix C) has been developed to determine the activation threshold of the selected parameter, *i.e.* the parameter value above which PRC is activated. In general, the input data of the algorithm include the measured DSD time-series for the LEE analyses, the standard and curtailed WT $N-V$ curves, and a user-given damage reduction, *i.e.* a target life extension. When the activation parameter is D_M, Algorithm A can use either the measured or Best DSD time-series to calculate the D_M threshold for activating PRC, but the LEE assessment is performed with measured DSD time-series. With minor alterations, Algorithm A has also been used to determine the curtailing threshold of R when using the measured rainfall rate to steer PRC.

Algorithm A determines the D_M or R thresholds for activating PRC in real-world operation. To assess the efficiency

of these curtailing thresholds, a second algorithm (Algorithm B in Appendix C) has been developed. Its aim is to determine, for given LE life extension, the minimum theoretical amount of AEP loss due to speed curtailment, independently of the PRC activation parameter. Reduced AEP losses predicted by Algorithm B would correspond to reductions of the curtailing time and/or increased curtailing below rated wind speed. The ratio between the AEP losses of Algorithms A and B is a measure of the efficiency of the considered curtailing parameter. Appendix C reports an analysis of the sensitivity of the PRC performance predicted by Algorithm A and the convergence characteristics of the algorithm to the main convergence tolerance parameter. The section also reports a study on the sensitivity of Algorithms A and B to the time-step of the rain data time-series.

3.4. LE life extension and AEP losses for speed curtailment

The LE of WTs operating in standard mode erode with time and, therefore, AEP decreases as time progresses. Using PRC, the progression of AEP losses due to LEE can be reduced or suppressed. However, an AEP loss due to rotor speed curtailment arises. An optimal PRC set-up should aim to minimize this loss while maximizing LE life. In the PRC analyses of this section, the AEP loss for rotor speed curtailment is estimated with respect to the ideal AEP with standard operation and nominal blades. These reference AEP values for the three sites are reported in Tab. 5. The presented analyses also investigate the impact of using alternative precipitation parameters to extend LE life while minimizing AEP losses for speed curtailment.

Table 8 shows the AEP losses and LEE lives for rotor speed curtailment of the 15 MW WT with and without PRC at the Lancaster site. Alternative PRC set-ups are considered, and the main operational parameters for each set-up are also provided. Each row refers to the PRC set-up indicated in the first column. For all PRC set-ups, the operating parameters have been determined by prescribing a target LEE life equal to twice that with standard operation. The second column, labeled 'Par_{curt}', provides the PRC activation threshold of the considered rain-related parameter ($D_{M,M}$ and $D_{M,B}$ are in [mm] and R is in [mm/hr]), and the third column reports the incubation time at 95% blade tip radius. The fourth and fifth columns report, respectively, the percentage time of the reference period in which the WT produces power, *i.e.* the total time with $3 < V < 25$ m/s, and the percentage time of the operational period in which PRC is active. The variable $(\text{AEP loss})_{\text{curt}}$ in the last column is the percentage AEP loss due to rotor speed curtailment.

In Tab. 8, the second row, labeled '$D_{M,M}$', refers to the case of PRC activation based on the D_M values determined from measured DSDs. The activation threshold has been determined setting $N_x = N_M$ in Algorithm A. The third row, labeled '$D_{M,B}$', refers to PRC activation based on the D_M values determined with the Best DSD based on measured R values. The activation threshold has been determined setting $N_x = N_B$ in Algorithm A.

Using the $D_{M,M}$ set-up, yields an activation threshold of about 0.72 mm, lower than the value of about 1 mm obtained with the $D_{M,B}$ set-up. This results in the curtailing time and AEP loss of set-up $D_{M,M}$ being larger than those experienced with set-up $D_{M,B}$. In the latter case, the AEP loss due to speed curtailment is 0.83% of the reference AEP, whereas the loss amounts to 1.41% in the former case. The reason for these differences is the wide variability of measured DSDs for given rainfall rate R. This feature is highlighted by the large data scatter in Fig. 6. The implication of this scatter on PRC is further discussed below.

Table 8: Operational parameters of different PRC set-ups and AEP losses for rotor speed curtailment at Lancaster site.

PRC set-up	Par_{curt}	Life [yr]	Time Operational [%]	PRC Enabled [%]	**$(\text{AEP loss})_{\text{curt}}$ [%]**
no PRC	-	1.0	85.1	-	**-**
$D_{M,M}$	0.72	2.0	85.1	5.0	**1.41**
$D_{M,B}$	1.01	2.0	85.1	2.9	**0.83**
R (meas)	0.75	2.0	85.1	2.9	**0.83**
Ideal (meas)	-	2.0	85.1	2.4	**0.71**

The row of Tab. 8 labeled 'R (meas)' refers to PRC activation based on the measured R values. The AEP loss of 0.83% equals that obtained with set-up $D_{M,B}$. This is because there is a one-to-one relation between $D_{M,B}$ and R, resulting in the two PRC set-ups being equivalent. The curve of Best DSD-based D_M versus R is shown in Fig. 10c. The last row of Tab. 8, labeled 'Ideal (meas)' gives the optimal PRC operating conditions determined with Algorithm B. The AEP loss of 0.71% is smaller than that determined by using the $D_{M,B}$- and R-based curtailing. However, the relatively small difference indicates that Algorithm A is well suited to determine PRC activation thresholds.

The main finding of the analyses above is that steering PRC using measured R values or D_M values based on the Best DSD and measured R enables achieving a target LE life extension with a lower AEP loss with respect to set-up $D_{M,M}$. This is because the erosion damage correlates better with R than measured DSD-based D_M. This is illustrated in Figures 10a and 10b, which plot the fractional damage of each 10-min rain interval against $D_{M,M}$ and $D_{M,B}$, respectively. The data scatter is larger in the former case, and this adversely impacts the capability of Algorithm A to determine a satisfactory PRC activation threshold using measured D_M time-series. This is illustrated by considering points A and B in Fig. 10a. Algorithm A will start by excluding from standard WT operation many points like A, characterized by large D_M but unexpectedly low fractional damage. This type of points are characterized by low R and DSDs with a large proportion of large droplets. More damaging precipitations, like that of point B, yielding large fractional damage but featuring high R values and DSDs with a large proportion of smaller droplets, will be considered later by Algorithm A. Therefore, the use of measured D_M for PRC yields a lower, more restrictive, activation threshold of this variable with respect to when the $D_{M,B}$ set-up is used. This is also illustrated by considering point A' and B' in Fig. 10b, which are the counterparts of points A and B. The $D_{M,B}$ representation of these two rain events shows a stronger correlation of fractional damage and D_M, an occurrence which enables to significantly reduce the AEP loss due to speed curtailing.

Due to the one-to-one relation between $D_{M,B}$ and R, the correlation between fractional damage and R is also quite strong, as shown in Fig. 10d.

In order to visualize the effect of PRC on the LEE damage reduction, Fig. 11 reports the joint FDF of fractional damage as function of R and V at the Lancaster site using PRC. The map should be compared with that of Fig. 9f referring to standard operation. In both figures, the horizontal black line denotes the PRC R activation threshold of 0.75 mm/hr. The map of Fig. 11 indicates substantial reductions of the fractional damage for $R > 0.91$ mm/hr, and notable reductions also in the range $0.45 < R < 0.91$ mm/hr, confirming the correctness and strength of the adopted approach.

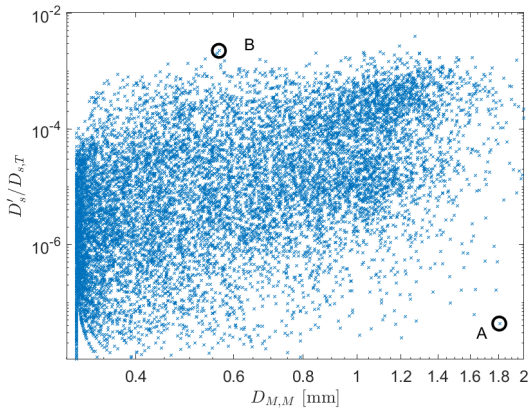

(a) Fractional damage accumulated in each 10-min interval of measured DSD time-series against measured DSD-based D_M.

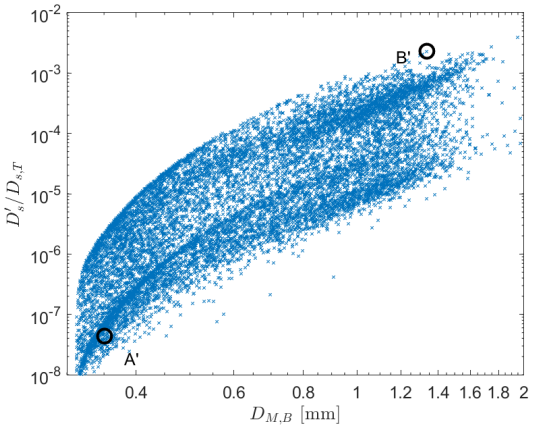

(b) Fractional damage accumulated in each 10-min interval of measured DSD time-series against Best DSD-based D_M.

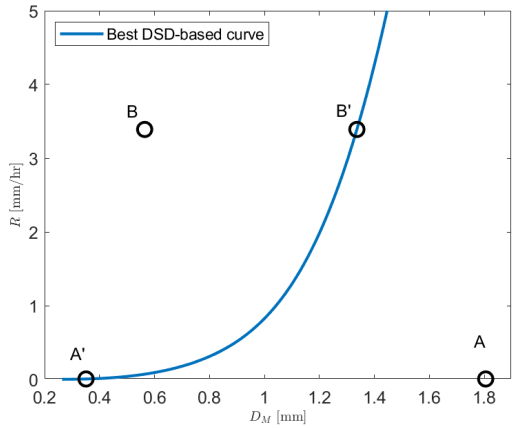

(c) Analytical relationship between R and D_M based on Best DSD.

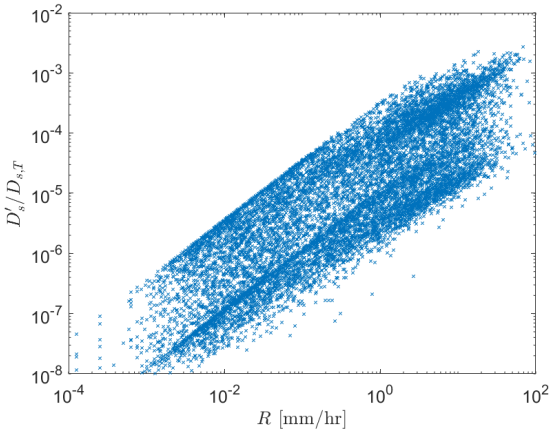

(d) Fractional damage accumulated in each 10-min interval of measured DSD time-series against measured DSD-based R.

Figure 10: Relations between fractional damage, D_M and R at Lancaster site, and Best DSD-based relation between R and D_M.

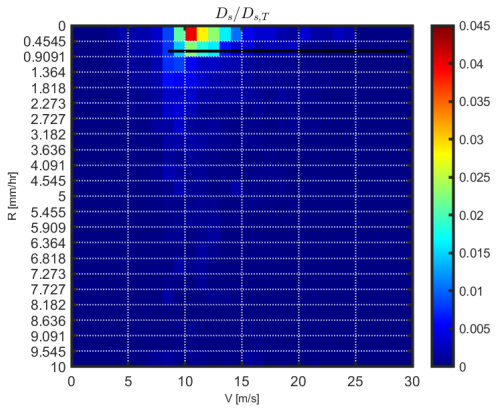

Figure 11: Fractional damage FDF based on V and R using R-based PRC.

Table 9: Operational parameters of different PRC set-ups and AEP losses for rotor speed curtailment at Lampedusa site.

PRC set-up	Par_{curt}	Life [yr]	Time Operational [%]	PRC Enabled [%]	**$(\text{AEP loss})_{\text{curt}}$ [%]**
no PRC	-	13.8	87.1	-	**-**
$D_{M,M}$	0.93	27.6	87.1	0.8	**0.21**
$D_{M,B}$	0.96	27.5	87.1	0.3	**0.07**
R (meas)	0.58	27.7	87.1	0.3	**0.07**
Ideal (meas)	-	27.7	87.1	0.2	**0.06**

All observations above also apply to the Lampedusa site. Table 9 summarizes the results of the PRC analyses of this site. All PRC set-ups double the LE life, bringing it to more than 27 years, a duration longer than expected WT life. The $D_{M,M}$ set-up yields a larger AEP loss than the $D_{M,B}$ set-up, as expected. Similarly to the Lancaster site, the R-based PRC steering gives the same AEP loss of the $D_{M,B}$ set-up. The minimum level of AEP loss for rotor speed curtailment at Lampedusa is only 0.07% of the nominal WT AEP. This result emphasizes the PRC potential to greatly reduce blade surface maintenance costs at the expense of very small AEP losses at sites characterized by moderate precipitation climates.

The last row of Tab. 9, referring to PRC yielding minimum possible AEP loss for curtailment, reports an AEP loss of 0.06%, close to the AEP loss of the $D_{M,B}$ and R set-ups. This confirms again the effectiveness of PRC algorithm A.

The results of the PRC analyses for the NS site are reported in Tab. 10. All assessments use the R time-series for the reference period obtained from IMERG, with rainfall rates assumed to be constant over three consecutive 10-min intervals, as the time-step of the IMERG time-series is 30 min. Best DSDs are used in Algorithm A to calculate the LE damage, as disdrometric measurements are not available for this site. The data of the second and third rows indicate that using R- or $D_{M,B}$-driven PRC to double the life of the LEP system incurs an AEP loss of 0.89% due to curtailment. This value is slightly larger than that of 0.83% at the Lancaster site. This is due to longer speed curtailing required to achieve the set life extension. In turn, this is because the percentage of intense precipitation with high wind speed at this site is higher than at the other two sites, as noted by comparing the map of Fig. 8e with those of Figures 8a and 8c.

Table 10: Operational parameters of different PRC set-ups and AEP losses for rotor speed curtailment at North Sea site.

PRC set-up	Par_{curt}	Life [yr]	Time Operational [%]	PRC Enabled [%]	**$(\text{AEP loss})_{\text{curt}}$ [%]**
no PRC	-	0.79	92.4	-	**-**
$D_{M,B}$	1.02	1.6	92.4	3.6	**0.89**
R (IMERG)	0.80	1.6	92.4	3.6	**0.89**
Ideal (Best)	-	1.6	92.4	3.3	**0.87**

Also at the NS site, the ideal PRC set-up yields the smallest AEP loss (0.87%, results in last row of Tab. 10), which confirms the effectiveness of Algorithm A.

The PRC assessment of the NS site may be affected by larger uncertainty than that of the other two sites, since the agreement between IMERG data and ground-based rain gauge measurements is geographical area-dependent, and the numerical values of the processed IMERG data depend on availability and reliability of ground-based gauge measurements for bias correction [41]. The IMERG predictions are often found to agree with ground-based observations at North Sea latitudes, where rain is not predominantly convective [42]. Conversely, the relatively coarse 30-min time resolution and 10 Km $\times$10 Km space resolution of IMERG make it harder to predict local precipitation at site where the rain is predominantly convective, due to the high space and time variability of this precipitation type. In line with this, the sensitivity analyses of Appendix C highlight better agreement of the PRC analyses based on IMERG and LPM rain data at Lancaster than at Lampedusa. Since the North Sea area is not dominated by convective rain, an acceptable quality of the IMERG data and reliability of the PRC analyses using these data is expected. A conclusive statement on this, however, will require surface-based precipitation data for further validation.

The PRC analyses above are computationally inexpensive: for the Lancaster site, Algorithm A performs 20 LEE analyses over the reference period (further detail in Tab. C.1). As the wall-clock time of one LEE analysis on one core of a XEON e3-1225 v3 4-core processor is about 6 sec, the runtime of the PRC analysis is 2 min.

3.5. Trade-offs of AEP losses due to LEE and rotor speed curtailment

Assessing the economic viability of PRC requires evaluating the net balance of AEP losses including losses for LEE and losses for rotor speed curtailment with and without PRC. Table 11 summarizes this analysis for the three sites. The reported mean total AEP loss is calculated over three years. In the cases without PRC, it is assumed that the AEP loss for moderate LEE (Tab. 6) starts at the end of the incubation period (determined in Subsection 3.2) and continues for one year. Thereafter, the AEP loss for severe erosion (Tab. 6) starts and lasts until the end of the third year. The sum of these losses is averaged over three years. In the case with PRC, the AEP loss for moderate LEE starts at the end of the delayed incubation period, and the rest of the AEP losses for LEE is accounted for as before. The AEP loss count includes also losses for rotor speed curtailment (Tables 8, 9 and 10). The last row of Tab. 11 also reports the LE erosion-free life, taken to be the end of the incubation period with or without PRC.

At Lancaster, the mean AEP loss with PRC is marginally smaller than that with standard operation, but the LE life is doubled, increasing from one to two years. Thus, the maintenance frequency reduction is a net benefit for LCOE

reduction. At Lampedusa, a very small AEP loss of 0.07% for rotor curtailment yields erosion-free operation over the entire WT lifetime, also contributing a net LCOE benefit for eliminating the need for blade surface maintenance. At the NS site, instead, the mean AEP loss with PRC is larger than that in standard operation, although with a LE life extension of 0.75 years. A conclusive answer on the PRC economic viability for this site type requires detailed long-term cost analyses.

	Lancaster		Lampedusa		North Sea	
	PRC	no PRC	PRC	no PRC	PRC	no PRC
Mean total AEP loss [%]	1.29	1.37	0.07	–	1.42	0.88
Erosion-free life [yr]	2.0	1.0	27.5	13.8	1.5	0.75

Table 11: Mean total AEP losses at three sites over three years.

4. Conclusions

This study has presented a comprehensive comparative assessment of the potential of the WT PRC technology to mitigate blade LEE at one onshore (Lancaster) and two offshore (Lampedusa and NS) wind farm sites in Western Europe, while minimizing AEP losses for LEE and rotor speed curtailment. The site climate-dependent performance of this new technology has thus been analyzed. AEP losses due to both LEE and rotor speed curtailment have been estimated, and their trade-offs have been investigated for a preliminary assessment of the site-dependent viability of PRC. The IEA Wind 15 MW WT has been used in all LEE and PRC investigations, covering a reference period of one year. Time-series of wind speed measured with cup, sonic or LiDAR anemometers and DSD and rainfall rate measured by disdrometers or satellite systems have been used.

The reported analyses highlight that the PRC effectiveness varies notably with the site climate. It decreases with the total annual precipitation and its percentage at high wind speeds. At Lancaster, the three-year mean AEP loss due to LEE with standard operation is 1.37%. That with PRC, including both the loss due to speed curtailment and that due to LEE, is slightly reduced, but the erosion-free LE life is doubled, achieving two years. The saving in blade maintenance is a net positive contribution to reduced LCOE. At Lampedusa, PRC enables achieving 25+ years of erosion-free operation at the expense of a small 0.07% AEP loss for rotor speed curtailment. At the NS site, the three-year mean AEP loss due to LEE with standard operation is 0.88%. That with PRC, however, is larger, and the LE durability is increased by 0.75 years. Estimating the net effect of PRC on the mean LCOE for this site requires long-term cost analyses.

The evaluation of the PRC effectiveness based on the trade-off analysis of AEP losses for LEE and speed curtailment is conservative, because newer LEP materials are likely to increase the durability of the LE, and AEP losses due to WT downtime for blade repair are not considered. Both circumstances reduce the multi-year mean overall AEP loss with PRC. It is also noted that comparable PRC-enabled LE life extensions have a larger impact on LCOE offshore than onshore, due to notably larger O&M costs in the former environment. The AEP loss trade-off analyses herein,

based on accurate measured climatic conditions and computed WT performance with different LEE states, provide a comprehensive reference to inform real-world PRC deployment.

An investigation into best suited rainfall parameters for steering PRC has concluded, surprisingly, that the mass-weighted mean diameter D_M based on the Best DSD evaluated with measured rainfall rates enables PRC to achieve a given LE life extension with lower AEP loss for speed curtailment with respect to when D_M is computed using measured DSDs. This is due to the poor correlation between rainfall rate and mass-weighted diameters based on disdrometric measurements. It has been found that the effectiveness of PRC also depends on the measurement frequency of rain data, particularly at sites with rapid variations of the rainfall rate, with the effectiveness increasing as the frequency increases. The report also provides prototype algorithms to estimate the performance and maximum theoretical efficiency of other candidate rain metrics to steer PRC, tools that will aid further work leading to the real-world deployment of PRC.

The PRC analyses herein focused on rain erosion. However, blade damage can also arise due to hail and other airborne particles. Seawater aerosols have been recently shown to contribute notably to LEE at coastal sites [7]; the importance of this agent for the offshore industry is prompting its investigation [43]. PRC and other WT adaptive control strategies will enable accounting for this and other LEE contributors as soon as reliable and computationally affordable modeling capabilities of the associated erosion mechanisms will become available.

Acknowledgement

This research received support from a) the UK Engineering and Physical Sciences Research Council, Grants EP/W524438/1 and EP/T518037/1; b) the ACTRIS (Aerosol, Clouds, and Trace Gases Research Infrastructure) and ICOS (Integrated Carbon Observation System) European Research Infrastructure, and ENEA's Electric System Research Programme, Project 1.5 "High efficiency buildings for the energy transition", funded by the Italian Ministry for the Environment and Energy Security, CUP I53C24003330001; c) the Sapienza University of Rome program "Bando Ricerca Scientifica 2023 Parte 2 - Medi e Piccoli", project CUP B83C23007080005; d) the project "RENEWEDGE", reference INNEST/2024/47, funded by the Valencian Innovation Agency (AVI), Generalitat Valenciana, Spain.

Mr. Thomas Collin is acknowledged for performing the computational fluid dynamics analyses of the FFA-W3-211 airfoil with and without LEE, and Mr. Sadil Doraymoray Badalge is acknowledged for developing the MATLAB wrapper used to implement the baseline PRC algorithm in this study. Dr. Virginia Ciardini and Dr. Damiano Sferlazzo are acknowledged for their support with acquisition and processing of the meteorological data of the Lampedusa weather station. A special tribute goes to the late Dr. Claudio Scarchilli, who initiated precipitation measurements with disdrometers at the Lampedusa Station.

Appendix A. Material properties of the LE coating used in this study

The LEP selected for the analyses of this study is a polyurethane material, namely a 3M liquid coating. The material properties of this LEP system, determined using WARET data and the DNV GL recommended practice [44],

are reported below. Their derivation is presented in [27]. The symbols used below are the same used to define the WARET data-based material properties of LE coatings proposed in [25], standardized in [44] and used in the study of [20]. These reports describe thoroughly the methodology based on the WARET approach to perform the LEE assessment of real-world WTs subjected to general wind and rain climates. When using this method, some intrinsic material properties known from conventional static measurements (*e.g.* material density and ultimate strength) are combined with WARET data to determine the erosion strength metrics needed to assess the durability of WTs operating in real-world conditions. The approach relies on correcting some parameters of Springer's model [26] by means of $V_e - N_e$ curves determined from WARET data. Suitable standardized statistical data processing is adopted to obtain the aforementioned corrections. As explained in Section 2.2, for given droplet impact speed V_e, the variable N_e provides the number of impacts per unit surface of droplets of given diameter leading to the end of the incubation period. The linear variation of V_e along each of the three swirling arms and the use of inspections at different times of the test enable the construction of the complete $V_e - N_e$ curve. The materials involved in the WARET are the LE coating (properties indicated by subscript c below), the LE substrate (properties indicated by subscript s below) and liquid water (properties indicated by subscript L below). The material properties known before the WARET are reported in Tab. A.1, where the impedance Z is given by $Z = \rho C$.

Table A.1: Coating, substrate and water droplet material properties.

Parameters	Coating		Substrate		Water	
Density [kg/m^3]	ρ_c	1100	ρ_s	1560	ρ_L	1000
Speed of sound [m/s]	C_c	1900	C_s	2098	C_L	1480
Acoustic impedance [kg/(m^{2}s)]	Z_c	2090000	Z_s	3272880	Z_L	1480000
Coating thickness [m]	h_c	0.000175				

The considered WARET campaign used a single droplet diameter of 2.25 mm. In order to use the erosion analysis method of [25], the slope m of the $V_e - N_e$ curve determined from the WARET data is needed. After selecting a point of the $V_e - N_e$ curve, here denoted by $((V_e)_{fit}, (N_e)_{fit})$, the following parameters, needed for general LEE analysis in real-world conditions, can also be determined: modified LEP erosion strength S_{ec} accounting for additional stress reflections in coating and substrate, equivalent raw erosion strength S_c of LEP corresponding to droplet diameter of the WARET, and average stress σ_0 in the coating. The values of these parameters, corresponding to $(V_e)_{fit}$=134 m/s and $(N_e)_{fit}$=234.6057 impacts/mm^2 are reported in Tab. A.2.

Table A.2: Values of erosion strength parameters and exponent m for d=2.25 mm based on WARET.

S_{ec} [GPa]	S_c [GPa]	$\left(\frac{S_{ec}}{\sigma_0}\right)$	m
1.7021	2.4248	12.5634	7.41

Appendix B. Verification of wind and rain records

To verify the reliability of the wind speed time-series used for the LEE and PRC analyses at the three sites, the associated wind speed frequency occurrence has been compared with that of the corresponding ERA5 time-series. Since the output frequency of the ERA5 reanalysis is 1 hr, a mean hourly wind speed for each set of six consecutive 10-min intervals for the Lancaster and NS sites, and 60 consecutive 1-min intervals for Lampedusa. These averages are then extrapolated at 150 m using the ERA5-based γ exponent of the power law. The comparison is reported in the left plots of Fig. B.1, which show that very good agreement is observed for all three sites.

At the Lancaster and Lampedusa sites, the Thies Clima^{TM} LPM, which has horizontal area of capture A of $45.6 \cdot 10^{-4}$ m^2, measures the droplet diameters in 22 classes from 0.125 mm, and the droplet terminal velocities in 20 classes from 0.0 m/s [31]. The measured DSD $N_M(D)$ for each 1-min interval is computed with:

$$N_M(D_i) = \frac{1}{A v_t(D) \Delta t} \frac{\Delta n_i}{\Delta D_i} \tag{B.1}$$

where D_i, ΔD_i and Δn_i are, respectively, the mean diameter, the width and the droplet number of the i^{th} droplet class, $v_t(D)$ is the terminal velocity of the droplets of the i^{th} class, and Δt=60 s. In Eq. (B.1) all diameters are in mm, A is in m^2, v_t is in m/s and N_M has units [mm^{-1}·m^{-3}]. Due to uncertainty affecting disdrometric measures of v_t [45], the measured 1-min droplet size and velocity data have been filtered before computing the N_M DSD. The filter [46] uses the empirical relationship between D and v_t [47]:

$$v_t(D) = 9.65 - 10.3 e^{-0.6D} \tag{B.2}$$

where D is in mm and v_t is in m/s. Droplets of diameter D with measured velocity above or below 50% of the v_t value given by Eq. (B.2) are filtered out. The value of v_t in Eq. (B.1) is also determined with Eq. (B.2). The filtered LPM data have been also used to calculate the R value for each 1-min measurement using the relation:

$$R = \frac{3.6 \cdot 10^{-3}}{A \Delta t} \sum_{i=1}^{22} \Delta n_i V_i \tag{B.3}$$

with Δt in [s], A in [m^2] and R in [mm/hr]. The symbol V_i denotes the volume of the drop with diameter D_i in [mm].

The R time-series at the Lancaster and Lampedusa site, have been calculated also with the 10-min rainfall records a tipping bucket rain gauge (ARG100, Campbell Scientific at Lancaster and Vaisala RG13 at Lampedusa). The R occurrence frequencies for the Lancaster site based on the LPM and tipping bucket data, both aggregated on hourly intervals, are in very good agreement, as seen in Fig. B.1b. Figure B.1d presents a similar comparison for the Lampedusa site. The agreement of the two curves is very good up to $R \approx 3$ mm/hr. For $3 < R < 4$ mm/hr, some discrepancies are noted, but the number of rain occurrence in this interval is rather low. These data highlight good reliability of the disdrometric data for the LEE and PRC analyses of this study.

The IMERG R occurrence analysis for the NS site, using 30-min records, is reported in Fig. B.1f. Interestingly, the number of precipitation events with high R values (above 4.0 mm/hr) is larger than for the other two sites.

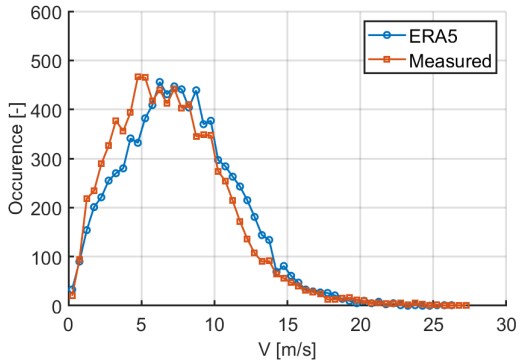

(a) Lancaster wind speed data.

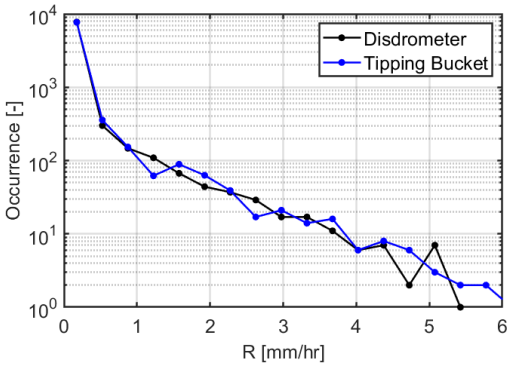

(b) Lancaster rainfall rate data.

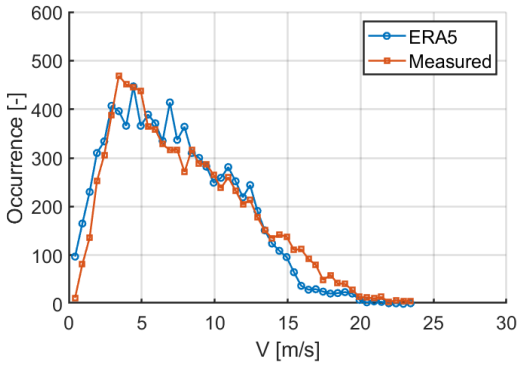

(c) Lampedusa wind speed data.

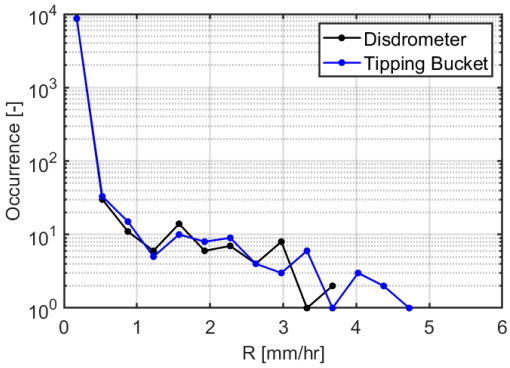

(d) Lampedusa rainfall rate data.

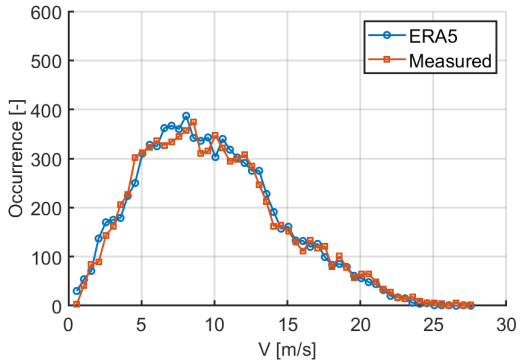

(e) North Sea site wind speed data.

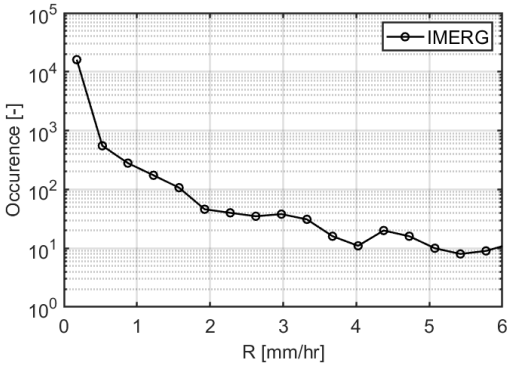

(f) North Sea site rainfall rate data.

Figure B.1: Left plots: comparison of wind speed occurrence frequency at three sites using anemometric and ERA5 time-series (anemometric data aggregated in hourly intervals). Top and middle right plots: comparison of R occurrence frequency at Lancaster and Lampedusa sites using disdrometric and tipping bucket time-series (both data aggregated in hourly intervals). Bottom right plot: R occurrence frequency at North Sea site based on IMERG time-series (30-min resolution).

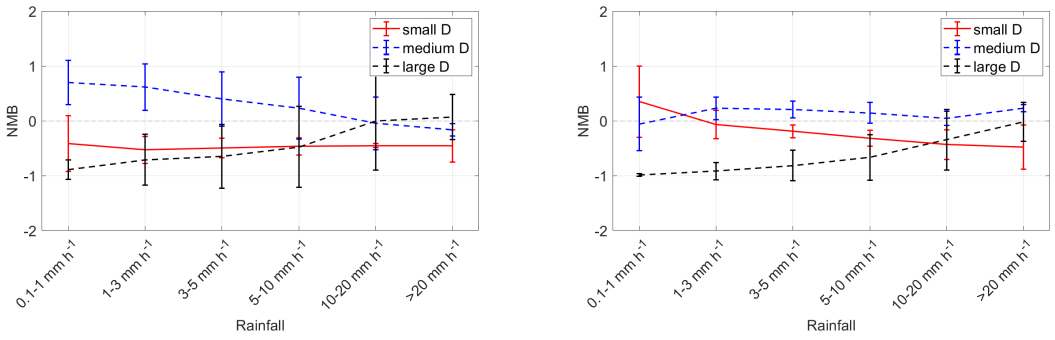

(a) NMB at Lancaster.

(b) NMB at Lampedusa.

Figure B.2: Normalized mean bias at Lancaster and Lampedusa sites.

The outcome of the D_M-based droplet size analyses reported in Fig. 6 can be better explained by considering the Normalized Mean Bias (NMB). For each of the classes D_i of droplet diameter, NMB is given by:

$$NMB_i = \frac{\sum_{t=1}^{N_t} [(N_B(D_i))_t - (N_M(D_i))_t]}{\sum_{t=1}^{N_t} (N_M(D_i))_t} \tag{B.4}$$

where t denotes the counter of the 1-min intervals with a precipitation, N_t is the total number of these intervals, and $N_M(D_i)$ and $N_B(D_i)$ denote, respectively, measured and Best DSD values of the t^{th} interval. The three NMB curves in the two plots of Fig. B.2 refer to small- (D <1 mm), medium- (1< D <3) mm, and large-size (D >3 mm) droplets; each curve reports the mean values of NMB for the R classes on the horizontal axis. For each 1-min interval, the Best DSD is evaluated using the measured R value. The reported NMB curves have been generated discarding disdrometric readings with $R < 0.1$ mm/hr and the first D class, corresponding to $0.125 < D < 0.250$, for all R values. This has been done to avoid the inaccuracy affecting disdrometric readings of very small droplet sizes. Figure B.2a highlights that the Best DSD significantly underestimates the amount of small droplets at all R levels at Lancaster. The amount of medium-sized droplets is instead overestimated for $R < 20$ mm/hr. The overprediction of this droplet size levels is often reported in the literature. It is also noted that the Best DSD also underpredicts the amount of large droplets, although the disdrometric records in this range may be less reliable than those for the medium-sized particles.

At Lampedusa (Fig. B.2b), the Best DSD predictions for small and medium-sized particles are closer to the measurements. This may be due to the different types of precipitation at the Lancaster and Lampedusa sites. At Lampedusa, more convective rain is expected, a precipitation type featuring relatively large droplet diameters.

Appendix C. PRC algorithms and sensitivity analyses

Algorithm A below determines the value of the mass-weighted mean diameter $D_{M,curt}$ above which, for $V > V_{curt} =$ 9 m/s, rotor speed curtailing is applied. The logical array PRC_{ON} has length M_I, and its entries are set to $true$ for all 10-min intervals with $D_M > D_{M,curt}$ and $V > V_{curt}$, turning on PRC. Algorithm A finds the value of $D_{M,curt}$ halving the total damage incurred without PRC. To this aim, the Secant method is used, with iterative step:

$$x_{n+1} = x_n - f(x_n)\frac{x_n - x_{n-1}}{f(x_n) - f(x_{n-1})} \tag{C.1}$$

In the pseudo-code below, $x = D_{M,curt}$ and $f(x) = F = D_{s,T}^{TAR} - \mathrm{TDW}(N_M, D_{M,curt}, V_{curt})$. Function TDW determines the entries of the logical array PRC_{ON} with function PRC_SWITCH, and then calls function TDam to get the total LEE damage accounting for PRC. The target total LEE damage $D_{s,T}^{TAR}$ is half the damage computed by function TDam without PRC, and the latter value is obtained by calling TDW with an unrealistically high value $D_{M,curt} = 10^3$ mm. Eq. (C.1) corresponds to the calculation of $D_{M,curt}^{new}$ in the pseudo-code, with subscripts $n+1$, n and $n-1$ replaced by superscripts *new*, 1 and 0. The convergence tolerance parameter $\Delta D_{M,min}$ for the analyses of Tables 8, 9 and 10 is set to 10^{-4}.

Algorithm B below determines the minimum theoretical AEP loss for given LE life extension and a single level of rotor speed curtailment, independently of the PRC activation parameter. In this method, speed curtailment is driven directly by the fractional damage D'_s and the method is only a benchmark for Algorithm A. Routine PDam determines the partial (*i.e.* fractional) damage array without PRC $(D'_s)^{NoPRC}$ for the M_I 10-min intervals with rain. Then, for $V > V_{curt}$, function PRC_SCALE divides each entry of $(D'_s)^{NoPRC}$ by the corresponding difference between the power P^{NoPRC} in standard operation and the power P^{PRC} with PRC. Since this difference is very small between V_{curt} and about 10 m/s, reaches its maximum at the rated wind speed of 11 m/s and remains at this level until cut-out, the scaled damage $(D'_s)^{NoPRC}_{scaled}$ between V_{curt} and the nominal wind speed is increased notably with respect to that at $V > 11$ m/s. Thereafter, the array $(D'_s)^{NoPRC}_{scaled}$ is sorted in order of decreasing values, storing the indices of the sorted array in the integer array IDX_{sorted}. Finally, PRC is applied to a progressively larger subset of the M_I intervals, starting from those with largest scaled damage. The damage scaling enables curtailing first the operation intervals with standard power output below the rated value, yielding reduced power loss for speed curtailing and minimizing the overall AEP loss. The algorithm stops when the subset to which PRC is applied enables meeting the target life extension.

In both algorithms, the time in which PRC is active is computed from the final estimate of array PRC_{ON}, multiplying by 10 minutes the sum of the entries set to $true$. Both algorithms also read in the power curves with and without PRC reported in Fig. 3. The AEP loss for speed curtailment is computed taking the difference of the AEP without and with PRC. Both values are computed using the V time-series (also read in), adding up the energy produced in each 10-min interval: the AEP without PRC is determined with the entire PRC_{ON} array set to $false$, and that with PRC is determined using the final values of array PRC_{ON}. These details are omitted in the pseudo-codes for brevity.

Table C.1 presents a study of the sensitivity of the physical output and the numerical performance of Algorithm A to the magnitude of $\Delta D_{M,min}$. The analysis refers to the Lancaster site and $D_{M,B}$-based PRC. The computed PRC activation threshold $D_{M,curt}$ and the AEP loss for speed curtailment are found to be independent of the magnitude of $\Delta D_{M,min}$ if this parameter is smaller than about $6 \cdot 10^{-3}$; 10 to 20 calls to TDW, the core analysis function of Algorithm A, are needed for convergence.

The sensitivity of the PRC performance to the time-step of the rain data is analyzed in Tables C.2 and C.3, which refer to the Lancaster and Lampedusa sites, respectively. The analyses refer to $D_{M,B}$-based rotor speed curtailment. The LEE and PRC analyses use a 10-min time-step in all cases, with the site-specific wind speed time-series. When using a 30-min step for the rain data, the measured disdrometric data over three consecutive 10-min interval, needed for the LEE analysis of function TDW, are obtained by averaging the disdrometric data of the corresponding three consecutive

Algorithm A. D_M-based PRC

$V_{curt} = 9$; $\Delta D_{M,min} = 10^{-4}$; $n = 1$; $n_{max} = 100$:

$D_{s,T}^{TAR} = 0.5 \times \text{TDW}(N_M, 10^3, V_{curt})$;

$D_{M,curt}^0 = 0.1$; $F^0 = D_{s,T}^{TAR} - \text{TDW}(N_M, D_{M,curt}^0, V_{curt})$

$D_{M,curt}^1 = 4$; $F^1 = D_{s,T}^{TAR} - \text{TDW}(N_M, D_{M,curt}^1, V_{curt})$

while $|D_{M,curt}^1 - D_{M,curt}^0| < \Delta D_{M,min}$ **do**

$D_{M,curt}^{new} = D_{M,curt}^1 - F^1 (D_{M,curt}^1 - D_{M,curt}^0)/(F^1 - F^0)$

$F^{new} = |D_{s,T}^{TAR} - \text{TDW}(N_M, D_{M,curt}^{new}, V_{curt})|$

if $F^{new} = 0$ — $n = n_{max}$ **then**

break

end if

$D_{M,curt}^0 = D_{M,curt}^1$; $F^0 = F^1$;

$D_{M,curt}^1 = D_{M,curt}^{new}$; $F^1 = F^{new}$; $n = n + 1$

end while

%

FUNCTION $D_{s,T}$ = TDW($N_M, D_{M,curt}, V_{curt}$)

PRC_{ON} = PRC_SWITCH($D_{M,curt}, V_{curt}$);

$D_{s,T} = \text{TDam}(N_M, PRC_{ON})$;

%

FUNCTION PRC_{ON} = PRC_SWITCH($D_{M,curt}, V_{curt}$)

for i=1:M_I **do**

Calculate $D_M(i)$ using $N_x(i)$; $PRC_{ON}(i) = \text{false}$

if $D_M(i) > D_{M,curt}$ & $V > V_{curt}$ **then**

$PRC_{ON}(i) = \text{true}$

end if

end for

Algorithm B. D_s'-based PRC (Ideal PRC)

$PRC_{ON} = false$; $D_{s,T}^{NoPRC} = \text{TDam}(N_M, PRC_{ON})$;

$(D_s')^{NoPRC} = \text{PDam}(N_M)$;

$V_{curt} = 9$;

$(D_s')_{scaled}^{NoPRC} = \ldots$

PRC_SCALE($(D_s')^{NoPRC}, V_{curt}, P^{NoPRC} - P^{PRC}$);

$[-, IDX_{sorted}] = sort((D_s')_{scaled}^{NoPRC})$;

$M_{curt} = 0$;

while $M_{curt} < M_I$ **do**

$M_{curt} = M_{curt} + 1$;

for i=1:M_{curt} **do**

$J_{PRC} = IDX_{sorted}(i)$;

$PRC_{ON}(J_{PRC}) = \text{true}$;

end for

$D_{s,T}^{PRC} = \text{TDam}(N_M, PRC_{ON})$;

if $D_{s,T}^{PRC} = 0.5 \times D_{s,T}^{NoPRC}$ **then**

break

end if

end while

10-min intervals of LPM measurements. The rainfall rate of the three 10-min intervals is obtained by averaging that measured by the LPM. At both sites, the performance of PRC worsens at the measuring interval of rain data increases, particularly at sites like Lampedusa, characterized by faster R variations.

Tab. C.4 reports the results of the PRC analysis for the Lancaster and Lampedusa sites using the IMERG R time-series and Best DSDs based on IMERG's R values. Since the time-resolution of IMERG is 30 minutes, the R value of three consecutive 10-min intervals in the PRC analyses have been set equal to the value of the corresponding 30-min IMERG interval. These results highlight a fairly good agreement between the IMERG-based PRC analysis and the LPM-based PRC analyses (Tab. C.2) for Lancaster, but substantial differences are found with respect to the LPM-based PRC analysis for Lampedusa (Tab. C.3). This is because IMERG significantly overestimates the precipitation level at

Lampedusa with respect to LPM measurements.

Table C.1: Sensitivity analysis of output and numerical performance of Algorithm A to magnitude of convergence tolerance parameter $\Delta D_{M,min}$. Results refer to Lancaster site and $D_{M,B}$-based PRC.

$\Delta D_{M,min}$ [mm]	$D_{M,curt}$ [mm]	Life [yr]	**(AEP loss)$_{curt}$ [%]**	# TDW calls
10^{-4}	1.0149	1.9924	0.8336	20
$8 \cdot 10^{-4}$	1.0148	1.9938	0.8349	15
$6.4 \cdot 10^{-3}$	1.0188	1.9821	0.8245	10
$5.12 \cdot 10^{-2}$	1.0000	2.0372	0.8732	5
0.1	1.0000	1.8907	0.7533	4

Table C.2: Sensitivity analysis of output of Algorithms A and B to time-step Δt of wind and rain time-series. Results refer to Lancaster site and $D_{M,B}$-based PRC.

Δt [min]	PRC set-up	$D_{M,curt}$ [mm]	Life [yr]	Time Op. [%]	PRC Enabled [%]	**(AEP loss)$_{curt}$ [%]**
10	no PRC	-	1.00	85.1	-	**-**
	$D_{M,B}$	1.01	2.00	85.1	2.9	**0.83**
	Ideal (meas)	-	2.00	85.1	2.4	**0.71**
30	no PRC	-	1.00	85.1	-	**-**
	$D_{M,B}$	0.92	2.00	85.1	3.7	**1.05**
	Ideal (meas)	-	2.00	85.1	2.7	**0.82**

Table C.3: Sensitivity analysis of output of Algorithms A and B to time-step Δt of wind and rain time-series. Results refer to Lampedusa site and $D_{M,B}$-based PRC.

Δt [mm]	PRC set-up	$D_{M,curt}$ [mm]	Life [yr]	Time Op. [%]	PRC Enabled [%]	**(AEP loss)$_{curt}$ [%]**
10	no PRC	-	13.8	87.1	-	**-**
	$D_{M,B}$	0.96	27.5	87.1	0.3	**0.07**
	Ideal (meas)	-	27.7	87.1	0.2	**0.06**
30	no PRC	-	14.1	87.1	-	**-**
	$D_{M,B}$	0.76	28.2	87.1	0.5	**0.14**
	Ideal (meas)	-	28.2	87.1	0.3	**0.08**

References

[1] G. Rinaldi, P. R. Thies, L. Johanning, Current status and future trends in the operation and maintenance of offshore wind turbines: A review, Energies 14 (9) (2021). doi:https://doi.org/10.3390/en14092484.

Table C.4: Results of $D_{M,B}$-based PRC analyses at Lancaster and Lampedusa sites using IMERG *R* time-series.

Site	PRC set-up	$D_{M,curt}$ [mm]	Life [yr]	Time Op. [%]	PRC Enabled [%]	**(AEP loss)$_{\mathbf{curt}}$ [%]**
Lancaster	no PRC	-	1.33	85.1	-	**-**
	$D_{M,B}$	1.11	2.66	85.1	2.3	**0.66**
	Ideal (Best)	-	2.66	85.1	2.0	**0.63**
Lampedusa	no PRC	-	4.00	87.1	-	**-**
	$D_{M,B}$	0.98	7.96	87.1	1.1	**0.29**
	Ideal (Best)	-	7.97	87.1	0.9	**0.28**

[2] R. Herring, K. Dyer, F. Martin, C. Ward, The increasing importance of leading edge erosion and a review of existing protection solutions, Renewable and Sustainable Energy Reviews 115 (2019) 109382. doi:https://doi.org/10.1016/j.rser.2019.109382.

[3] M. Campobasso, A. Castorrini, L. Cappugi, A. Bonfiglioli, Experimentally validated three-dimensional computational aerodynamics of wind turbine blade sections featuring leading edge erosion cavities, Wind Energy 25 (1) (2022) 168–189. doi:https://doi.org/10.1002/WE.2666.

[4] A. Castorrini, A. Ortolani, M. S. Campobasso, Assessing the progression of wind turbine energy yield losses due to blade erosion by resolving damage geometries from lab tests and field observations, Renewable Energy 218 (2023) 119256. doi:https://doi.org/10.1016/j.renene.2023.119256.

[5] M. S. Campobasso, A. Castorrini, A. Ortolani, E. Minisci, Probabilistic analysis of wind turbine performance degradation due to blade erosion accounting for uncertainty of damage geometry, Renewable and Sustainable Energy Reviews 178 (2023) 113254. doi:https://doi.org/10.1016/j.rser.2023.113254.

[6] L. Cappugi, A. Castorrini, A. Bonfiglioli, E. Minisci, M. Campobasso, Machine learning-enabled prediction of wind turbine energy yield losses due to general blade leading edge erosion, Energy Conversion and Management 245 (2021) 114567. doi:https://doi.org/10.1016/j.enconman.2021.114567.

[7] H. Law, V. Koutsos, Leading edge erosion of wind turbines: Effect of solid airborne particles and rain on operational wind farms, Wind Energy 23 (10) (2020) 1955–1965. doi:https://doi.org/10.1002/we.2540.

[8] K. Panthi, G. V. Iungo, Quantification of wind turbine energy loss due to leading-edge erosion through infrared-camera imaging, numerical simulations, and assessment against SCADA and meteorological data, Wind Energy 26 (3) (2023) 266–282. doi:https://doi.org/10.1002/we.2798.

[9] L. Mishnaevsky Jr., K. Thomsen, Costs of repair of wind turbine blades: Influence of technology aspects, Wind Energy 23 (12) (2020) 2247–2255. doi:https://doi.org/10.1002/we.2552.

[10] J. McMorland, C. Flannigan, J. Carroll, M. Collu, D. McMillan, W. Leithead, A. Coraddu, A review of operations

and maintenance modelling with considerations for novel wind turbine concepts, Renewable and Sustainable Energy Reviews 165 (2022) 112581. doi:https://doi.org/10.1016/j.rser.2022.112581.

[11] RE News, London Array braced for blade fix, renews.biz/110465/%20london-array-braced-for-blade-%EF%AC%81x, accessed on 28 November 2022 (2018).

[12] RE News, Anholt grapples with blade fix, renews.biz/110279/anholtgrapples-with-blade-%EF%AC%81x, accessed on 28 November 2022 (2018).

[13] A. Ning, K. Dykes, Understanding the Benefits and Limitations of Increasing Maximum Rotor Tip Speed for Utility-Scale Wind Turbines, Journal of Physics: Conference Series 524 (2014) 012087.

[14] J. Bech, C. Hasager, C. Bak, Extending the life of wind turbine blade leading edges by reducing the tip speed during extreme precipitation events, Wind Energy Science 3 (2) (2018) 729–748. doi:https://doi.org/10.5194/wes-3-729-2018.

[15] S. C. Pryor, J. J. Coburn, R. J. Barthelmie, Spatiotemporal variability in wind turbine blade leading edge erosion, Energies 18 (2) (2025). doi:10.3390/en18020425.

[16] F. Letson, S. C. Pryor, From Hydrometeor Size Distribution Measurements to Projections of Wind Turbine Blade Leading-Edge Erosion, Energies 16 (9) (2023). doi:10.3390/en16093906.

[17] J. Fang, W. Hu, Z. Liu, W. Chen, J. Tan, Z. Jiang, A. S. Verma, Wind turbine rotor speed design optimization considering rain erosion based on deep reinforcement learning, Renewable and Sustainable Energy Reviews 168 (2022) 112788. doi:https://doi.org/10.1016/j.rser.2022.112788.

[18] W. Hu, W. Chen, X. Wang, Z. Jiang, Y. Wang, A. S. Verma, J. J. Teuwen, A computational framework for coating fatigue analysis of wind turbine blades due to rain erosion, Renewable Energy 170 (2021) 236–250. doi:https://doi.org/10.1016/j.renene.2021.01.094.

[19] J. I. Bech, N. F.-J. Johansen, M. B. Madsen, Ásta Hannesdóttir, C. B. Hasager, Experimental study on the effect of drop size in rain erosion test and on lifetime prediction of wind turbine blades, Renewable Energy 197 (2022) 776–789. doi:https://doi.org/10.1016/j.renene.2022.06.127.

[20] A. Castorrini, V. F. Barnabei, L. Domenech, A. Šakalyté, F. Sánchez, M. S. Campobasso, Impact of meteorological data factors and material characterization method on the predictions of leading edge erosion of wind turbine blades, Renewable Energy 227 (2024) 120549. doi:https://doi.org/10.1016/j.renene.2024.120549.

[21] A. C. Best, The size distribution of raindrops, Quarterly Journal of the Royal Meteorological Society 76 (327) (1950) 16–36. doi:https://doi.org/10.1002/qj.49707632704.

[22] E. Gaertner, J. Rinker, L. Sethuraman, F. Zahle, B. Anderson, G. Barter, N. Abbas, F. Meng, P. Bortolotti, W. Skrzypinski, G. Scott, R. Feil, H. Bredmose, K. Dykes, M. Shields, C. Allen, A. Viselli, Definition of the IEA Wind 15-Megawatt Offshore Reference Wind Turbine, Tech. Rep. NREL/TP-5000-75698, NREL, Golden, CO, USA (March 2020).

[23] J. Jonkman, M. Sprague, OpenFAST: An aeroelastic computer-aided engineering tool for horizontal axis wind turbines, www.nrel.gov/wind/nwtc/openfast.html, national Renewable Energy Laboratiry, Golden, Colorado. Accessed on 30 July 2025.

[24] NREL, ElastoDyn Users Guide and Theory Manual, https://openfast.readthedocs.io/en/dev/source/user/elastodyn/index.html, national Renewable Energy Laboratiry, Golden, Colorado. Accessed on 30 July 2025.

[25] D. Eisenberg, S. Laustsen, J. Stege, Wind turbine blade coating leading edge rain erosion model: Development and validation, Wind Energy 21 (10) (2018) 942–951.

[26] G. S. Springer, C.-I. Yang, P. S. Larsen, Analysis of rain erosion of coated materials, Journal of Composite Materials 8 (3) (1974) 229–252.

[27] F. Sánchez, H. Hao, L. Domenech, Y. Hardalupas, V. García, M. Charalambides, M. Ibáñez Arnal, A. Sergis, A. Taylor, A review and assessment of the rain erosion damage initiation of wind turbine blades leading edge protection systems based on laboratory testing data and industrial recommended practice DNVGL-RP-0573 (March 2025). doi:https://dx.doi.org/10.2139/ssrn.5165106.

[28] H. Hersbach, B. Bell, P. Berrisford, S. Hirahara, A. Horányi, J. Muñoz-Sabater, J. Nicolas, C. Peubey, R. Radu, D. Schepers, A. Simmons, C. Soci, S. Abdalla, X. Abellan, G. Balsamo, P. Bechtold, G. Biavati, J. Bidlot, M. Bonavita, G. De Chiara, P. Dahlgren, D. Dee, M. Diamantakis, R. Dragani, J. Flemming, R. Forbes, M. Fuentes, A. Geer, L. Haimberger, S. Healy, R. J. Hogan, E. Hólm, M. Janisková, S. Keeley, P. Laloyaux, P. Lopez, C. Lupu, G. Radnoti, P. de Rosnay, I. Rozum, F. Vamborg, S. Villaume, J.-N. Thépaut, The ERA5 global reanalysis (2020). doi:https://doi.org/10.1002/qj.3803.

[29] W. Watson, S. Zwick, M. Jonietz Alvarez, G. Wolken-Möhlmann, BSH N9 floating lidar measurement campaign - report for the measurement period 2022-03-03 to 2023-06-15, Tech. rep., Fraunhofer-Institute for Wind Energy Systems IWES, Bremerhaven, Germany (2024).

[30] NASA, IMERG: Integrated Multi-satellitE Retrievals for GPM, https://gpm.nasa.gov/data/imerg, accessed on 30 August 2025.

[31] THIES-Clima, Laser Precipitation Monitor, https://www.thiesclima.com/db/dnl/5.4110.xx.x00_Laser_Precipitation_Monitor_eng.pdf, Adolf Thies GmbH, Göttingen, Germany. Accessed on 30 July 2025.

[32] R. Herring, K. Dyer, P. Howkins, C. Ward, Characterisation of the offshore precipitation environment to help combat leading edge erosion of wind turbine blades, Wind Energy Science 5 (4) (2020) 1399–1409. doi:https://doi.org/10.5194/wes-5-1399-2020.

[33] B. Amirzadeh, A. Louhghalam, M. Raessi, M. Tootkaboni, A computational framework for the analysis of rain-induced erosion in wind turbine blades, part I: Stochastic rain texture model and drop impact simulations, Journal of Wind Engineering and Industrial Aerodynamics 163 (2017) 33–43. doi:https://doi.org/10.1016/j.jweia.2016.12.006.

[34] J. Nikuradse, Laws of flow in rough pipes, Technical Memorandum NASA TM 1292, Lewis Research Center, Washington, USA (November 1950).

[35] Ansys-Inc, Fluent theory guide, release 2024.r2, www.ansys.com/Products/Fluids/ANSYS-Fluent, accessed on 15 August 2025 (2024).

[36] F. Menter, Two-equation Turbulence-models for Engineering Applications, AIAA Journal 32 (8) (1994) 1598–1605.

[37] R. Langtry, F. Menter, Correlation-Based Transition Modeling for Unstructured Parallelized Computational Fluid Dynamics Codes, AIAA Journal 47 (12) (2009) 2894–2906.

[38] A. Tokay, W. A. Petersen, P. Gatlin, M. Wingo, Comparison of Raindrop Size Distribution Measurements by Collocated Disdrometers, Journal of Atmospheric and Oceanic Technology 30 (8) (2013) 1672 – 1690. doi:https://doi.org/10.1175/JTECH-D-12-00163.1.

[39] M. Angulo-Martínez, S. Beguería, B. Latorre, M. Fernández-Raga, Comparison of precipitation measurements by OTT Parsivel^2 and Thies LPM optical disdrometers, Hydrology and Earth System Sciences 22 (5) (2018) 2811–2837. doi:https://doi.org/10.5194/hess-22-2811-2018.

[40] A. Guyot, J. Pudashine, A. Protat, R. Uijlenhoet, V. R. N. Pauwels, A. Seed, J. P. Walker, Effect of disdrometer type on rain drop size distribution characterisation: a new dataset for south-eastern Australia, Hydrology and Earth System Sciences 23 (11) (2019) 4737–4761. doi:https://doi.org/10.5194/hess-23-4737-2019.

[41] A. Navarro, E. García-Ortega, A. Merino, J. L. Sánchez, C. Kummerow, F. J. Tapiador, Assessment of imerg precipitation estimates over europe, Remote Sensing 11 (21) (2019). doi:10.3390/rs11212470.

[42] T. Ivanova, A. Palatos-Plexidas, S. Porchetta, S. Buckingham, J. v. Beeck, L. D. Cruz, J. Helsen, W. Munters, Precipitation conditions in offshore wind farm zones: Insights from satellites and weather simulations, Journal of Physics: Conference Series 3131 (1) (2025) 012005. doi:10.1088/1742-6596/3131/1/012005.

[43] H. Sista, A. Dhulipalla, A. Kumar, H. Hu, H. Hu, A Comparative Study to Examine Rain Erosion Characteristics Upon Impingements of Freshwater and Saltwater Droplets Pertaining to Offshore Wind Turbine Operation",

howpublished = ”AIAA paper 91-1596, AIAA Aviation Forum and ASCEND 2025, Las Vegas, Nevada (July 2025).

[44] DNV-RP-0573, Evaluation of erosion and delamination for leading edge protection systems of rotor blades, https://standards.dnv.com/explorer/document/33994B586F7043EFAFA72320E11687BE.

[45] A. Tokay, D. B. Wolff, W. A. Petersen, Evaluation of the New Version of the Laser-Optical Disdrometer, OTT Parsivel2, Journal of Atmospheric and Oceanic Technology 31 (6) (2014) 1276 – 1288. doi:https://doi.org/10.1175/JTECH-D-13-00174.1.

[46] E. Adirosi, F. Porcù, M. Montopoli, L. Baldini, A. Bracci, V. Capozzi, C. Annella, G. Budillon, E. Bucchignani, A. L. Zollo, O. Cazzuli, G. Camisani, R. Bechini, R. Cremonini, A. Antonini, A. Ortolani, S. Melani, P. Valisa, S. Scapin, Database of the Italian disdrometer network, Earth System Science Data 15 (6) (2023) 2417–2429. doi:https://doi.org/10.5194/essd-15-2417-2023.

[47] D. Atlas, R. C. Srivastava, R. S. Sekhon, Doppler radar characteristics of precipitation at vertical incidence, Reviews of Geophysics 11 (1) (1973) 1–35.